Full title: Low computational cost stochastic Gassmann fluid substitution modelling of hydrogen and carbon dioxide in clastic storage reservoirs

Abbreviated title: Seismic Response of H2 & CO2 in Clastic Reservoirs

Authors: Hector G. Barnett[1]*, Mark T Ireland[1], Charles K Dunham[1], Cees van der Land[1],

Author Affiliations: School of Natural and Environmental Sciences, Newcastle University, Newcastle upon Tyne, United Kingdom

Correspondence: h.barnett2@ncl.ac.uk

ORCID:

H.G.B https://orcid.org/0000-0003-2506-5524

M.T.I https://orcid.org/0000-0001-9777-0447

C.D https://orcid.org/0009-0004-1071-8320

C.V.D.L https://orcid.org/0000-0002-0301-6927

PREPRINT STATEMENT

This manuscript has not been peer-reviewed, it has been submitted to EarthArXiv as a preprint. A subsequent version of this manuscript may have slight edits and changes present. This manuscript has been submitted for publication in Geoenergy. If accepted, the final version of this manuscript will be available via the 'Peer-reviewed Publication DOI' link on the right-hand side of this webpage.

1.1 Abstract

The ability to safely store non-hydrocarbon fluids in the subsurface, such as carbon dioxide or hydrogen, will likely be vital in all pathways to decarbonise global energy systems. Storage of these fluids will require monitoring programmes to identify dynamic changes during the injection and storage phases and to identify unintended migration. Seismic monitoring is widely adopted in monitoring plans. We investigate the changes in seismic response for different non-hydrocarbon fluids and different saturations.

The bulk elastic properties of subsurface rocks are influenced by the fluids present within the pore space and impact the seismic response of the rock. We undertake fluid substitution modelling, calculating new rheological properties of reservoir intervals after substituting brine for either hydrogen or carbon dioxide, varying the water saturation from 100% to 0%, and determining the new elastic properties. We investigate three proposed reservoirs for carbon dioxide storage on the UKCS, the Triassic Bunter Sandstone Formation, the Permian Leman Sandstone Formation and the Triassic Helsby (Ormskirk) Sandstone Formation. The workflow is stochastic and as such allows for the investigation of the impact of geological uncertainty on the results. The newly determined elastic properties are then used for modelling the seismic response and wedge models.

1.2 Introduction

Pore-filling fluids within a reservoir modify the bulk elastic properties and consequently impact the seismic response (Mavko et al., 2009). Forward modelling of the seismic response of porous reservoirs with different pore-filling fluids is commonplace within hydrocarbon exploration and production workflows where it is used to understand the expected seismic response of the subsurface (Avseth et al., 2005). In recent years these methods have been used to model carbon dioxide with respect to carbon capture storage (CCS) projects (Dupuy et al., 2017; Carpentier et al., 2021; Harvey et al., 2022b), and can be considered applicable to hydrogen storage also.

The seismic response of a geological boundary can be described by the reflection coefficient of the interface, which is determined by the acoustic impedance of the two layers, defined as: (Bacon et al., 2003);

$$\mathrm{Rc} = \frac{\mathrm{Ai}_2 - \mathrm{Ai}_1}{\mathrm{Ai}_2 + \mathrm{Ai}_1} \qquad \textit{Equation 1}$$

$$\mathrm{Ai} = \rho_{\mathrm{bulk}} * \mathrm{v_p} \qquad \textit{Equation 2}$$

Where Ai_1 and Ai_2 are the acoustic impedance values for the reservoir layers above and below the geological boundary, and where ρ_{bulk} is the bulk density of the reservoir layer and V_p is the compressional velocity. Both the bulk density and compressional velocity of a reservoir is modified by the pore-filling fluid. As different fluids have different properties, the extent to which the bulk density and compressional velocity of a reservoir are modified depends on the constituent properties of the filling liquid (Batzle and Wang, 1992). Forward modelling the seismic response and comparing it with the actual seismic response allows for the prediction of the fluid or fluid mixture present within the pore space at the time of acquisition (Ahmed et al., 2015). The change in pore filling fluid will impact the amplitude of seismic response at different seismic wave offsets. Changes in elastic properties hence modify the reflection response, which can be interpreted to identify changes in fluid saturation (Wandler et al., 2007). These approaches are used for both hydrocarbon exploration and production, where changes in fluid distribution as a result of production can be detected, and for subsurface storage, where, changes in fluid distribution due to injection can be detected (Chadwick et al., 2005; Singer et al., 2018). In recent years there have been numerous studies that extend conventional fluid prediction methods to make use of computationally more complex methods, such as Bayesian inversion (e.g and Pradhan et al. (2020)). While these methods can be valuable, computationally low-cost Monte Carlo methods allow for rapid and easy hypothesis testing and do not require *a priors*, instead relying on observed data to determine the input parameters (Mosegaard, 2023). As such stochastic models can be used to distinguish between differing geological models (Ringrose and Bentley, 2021).

In this paper, we use a stochastic implementation of the Gassmann equations to undertake fluid substitutions in three reservoir intervals on the United Kingdom Continental Shelf (UKCS). We consider both carbon dioxide and hydrogen, determine the new elastic properties and model the expected seismic responses for different component parts of a storage complex (Figure 1).

Throughout this work we implement low computational cost techniques focussing on: Resource-Efficiency, where computational methods are designed and implemented to minimise resource usage. Approximate technique utilisation, where precision within calculations is traded for speed by using approximations. Data minimisation, only undertaking calculations on the data of interest.

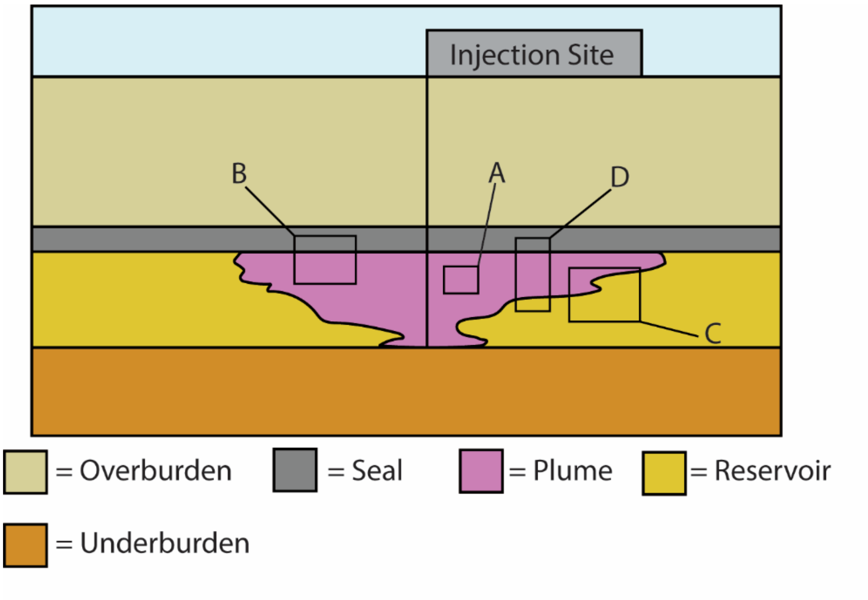

FIGURE 1. SCHEMATIC SUBSURFACE DIAGRAM OF A FLUID STORAGE SITE IN A POROUS RESERVOIR (NOT TO SCALE). BLACK BOXES REPRESENT AREAS WHICH ARE FORWARD MODELLED, A) RESERVOIR PROPERTIES B) SEAL - RESERVOIR INTERFACE, C) RESERVOIR (INJECTED FLUID SATURATED) – RESERVOIR (BRINE SATURATED) INTERFACE, D) WHOLE RESERVOIR COLUMN. PLUME TRACED FROM QUEST CCS FACILITY 2050 MODEL (HARVEY ET AL., 2022A).

1.3 Geological Setting

We undertake seismic modelling of three discrete reservoir – seal pairs from the UKCS. The chosen reservoir-seal pairs are located within two separate basins. The pairs from the Southern North Sea, the Bunter and Leman Sandstone, are located within the UK sector of the South Permian Basin, while the Helsby Sandstone is located within the Foryd-Gograth sub-basin of the East Irish Sea Basin (Ziegler, 1990; Jack et al., 1995). The South Permian Basin is an east-west trending basin, stretching from the eastern coast of the United Kingdom across Northern Europe to western Poland. Its formation is primarily attributed to mid-to-late Permian rifting events with modification from later phases of rifting and thermal subsidence. Its structural configuration was significantly influenced by the pre-existing tectonic framework established during the early Palaeozoic (Ziegler, 1992; Glennie, 1998; Glennie and Underhill, 1998). The East Irish Sea Basin is part of a Permo-Triassic rift system, consisting of northwest-southeast trending normal faults which control the basin architecture. A east-west trending horst graben system is responsible for the many sub-basins within the area including the Foryd-Gograth sub basin (Jack et al., 1995). Each of the reservoir intervals modelled has an associated planned CCS project (Gluyas and Bagudu, 2020; Clery and Gough, 2022; de Jonge-Anderson and Underhill, 2022; Gibson-Poole et al., 2024).

The Bunter Sandstone Formation is part of the Sherwood Sandstone Group and was deposited during the Olenekian of the Lower Triassic (Figure 2) (Bachmann et al., 2010). It consists of coarse-grained sandstones deposited in alluvial fan and fluvial environments in arid and semi-arid environments (Brook et al., 2003). It is overlain by the Haisborough group, which consists of a number of sealing formations, including claystone intervals and the Röt Halite (Bentham et al., 2013). The Zechstein supergroup, which the Sherwood Sandstone Group overlies, has undergone significant halokinesis, forming numerous salt domes and diapirs (Peryt et al., 2010). The mobilisation of the underlying Zechstein has caused several trap geometries to form within the Sherwood Sandstone Group of the Southern Permian Basin, one of which, known as the Endurance structure, was awarded the first UK carbon storage permit in December 2024 (James et al., 2016a; Gibson-Poole et al., 2024; UK Government, 2024).

The Helsby Sandstone Formation is part of the Sherwood Sandstone Group (Figure 2), it is also known as the Ormskirk Sandstone Formation depending on the nomenclature used**.** It is encountered throughout the East Irish Sea Basin (Kirk, 2005). It is early Triassic in age, having been deposited during the Anisian (Howard et al., 2008). It was deposited in a fluvial environment setting with aeoline influences, with facies of aeolian dunes and sandsheets present (Yaliz and Taylor, 2003; Scorgie et al., 2021). It is a reservoir for a number of gas fields within the East Irish Sea, with notable inclusions being the Hamilton field and Calder field (Yaliz and Taylor, 2003; Blow and Hardman, 2022).

The Leman Sandstone Formation is part of the Rotliegend group and is an Early Permian (Guadalupian - Lopingian) aged sedimentary succession consisting mainly of Aeolian sediments (Figure 2) (Gast et al., 2010). The Rotliegend group is found extensively throughout the South Permian Basin of Northern Europe, stretching from the east coast of the United Kingdom to the eastern edges of the Polish trough in Ukraine (Gast et al., 2010). It is the main gas-bearing reservoir within the UK sector of the South Permian Basin, where it is sealed by the Zechstein evaporite supergroup (Rouillard et al., 2020). The Rotliegend is also the reservoir used for the Rough gas storage field, where 54 BCF of natural gas is stored (Stuart, 1991).

It should be noted that within literature the lithostratigraphic nomenclature of the UKCS for different geological intervals can be varied and confusing, with different names being used for the same intervals. As such, we have followed the nomenclature set out by the British Geological Survey (2020) lexicon for the naming of reservoir intervals investigated.

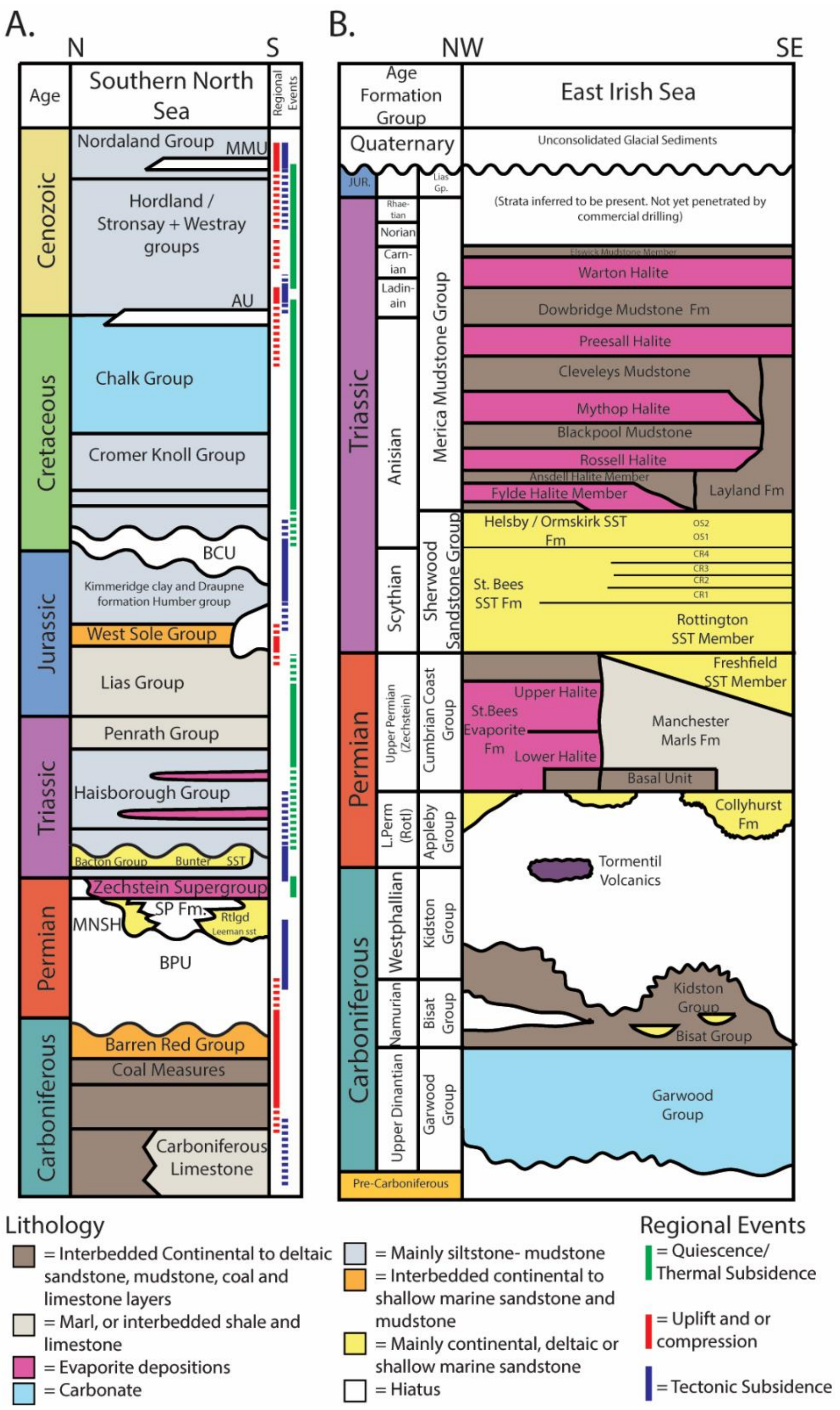

FIGURE 2 SOUTHERN NORTH SEA (A) AND EAST IRISH SEA (B) CHRONOSTRATIGRAPHIC DIAGRAM. A MODIFIED AFTER PATRUNO ET AL. (2022), B MODIFIED AFTER PATRONI ZAVALA ET AL. (2020)

1.4 Methodology

1.4.1 Fluid substitution

Fluid substitution is the property modelling of a rock, with the pore-filling fluid having been replaced by a new fluid or new ratios of two or more different fluids (Dvorkin et al., 2007). Fluid substitution modelling is commonly used to understand how the constituent properties of the rock are modified when alternative fluids to the original fill the pore space (Nolen-Hoeksema, 2000). The Gassmann equations are the most commonly used methodology to for fluid substitution modelling (Gassmann, 1951; Smith et al., 2003). The equations relate the bulk modulus of the saturated rock, K_{sat}, the bulk modulus of the dry rock frame, K^*, the bulk modulus of the mineral matrix, K_o, the porosity of the rock, Φ, and pore filling fluids bulk modulus, K_{fl} (Smith et al., 2003);

$$K_{sat} = K^* + \frac{(1 - \frac{K^*}{K_O})^2}{\frac{\Phi}{K_{fl}} + \frac{(1 - \Phi)}{K_O} - \frac{K^*}{K_O^2}}$$

EQUATION 3 – GASSMANN EQUATION

1.4.1.1 Bulk elastic rock properties

The bulk modulus of a saturated rock can be calculated using the compressional velocity, V_p, the shear velocity, V_s and the bulk density, ρ_{bulk} as;

$$K_{sat} = \rho_{bulk}(Vp^2 - \frac{4}{3}Vs^2)$$

EQUATION 4 – BULK MODULUS

Compressional velocity and shear velocity data can be obtained from either wireline logging or core measurements for a specific formation. We use data derived from well logs. Where the data are recorded as slowness (us/ft) a conversion into velocity is required;

$$Vp\left(\frac{m}{sec}\right) = 10^6 * 0.3048 * \text{Sonic Log(us/ft)}$$

EQUATION 5 – VELOCITY COMPRESSIONAL FROM SONIC COMPRESSIONAL LOG DATA

$$Vs\left(\frac{m}{sec}\right) = 10^6 * 0.3048 * \text{Shear Log(us/ft)}$$

EQUATION 6 – VELOCITY SHEAR FROM SHEAR SLOWNESS LOG

1.4.2 Fluid physical properties

Physical properties for pore filling fluids for substitution into the pore space may be determined from laboratory experiments (Salemi et al., 2018) or calculated theoretically using equations of state (EoS) (Danesh, 1998). In this study, the fluid's physical properties were calculated using the EoS models in the NIST Chemistry WebBook (1997). NIST used the following equations of state, carbon dioxide (Span and Wagner, 1996), hydrogen (Leachman et al., 2009), methane (Setzmann and Wagner, 1991). Reservoir conditions for the Helsby Sandstone reservoir were taken from Yaliz and Taylor (2003), conditions for the Leman were taken from Anston-Race and Ganesh (2020), and conditions for the Bunter Sandstone were taken from Gluyas and Bagudu (2020) (**Error! Reference source not found.**).

We assume carbon dioxide and hydrogen are in the supercritical phase at the described reservoir conditions (NIST Chemistry WebBook, 1997; Okere et al., 2024) (Table 1), for methane we model a pure dry pure system.

The bulk modulus of a fluid was calculated using the bulk density and speed of sound through the medium as;

$$K_{fl} = \rho * v^2$$

EQUATION 7 – BULK MODULUS OF FLUID

1.4.2.1 The Gassmann Equations

The Gassmann equation related the bulk modulus of the dry rock frame to the properties of rocks in given in situ conditions,

$$K^* = \frac{K_{sat}\left(\frac{\Phi K_o}{K_{fl}} + 1 - \Phi\right) - K_o}{\frac{\Phi K_o}{K_{fl}} + \frac{K_{sat}}{K_o} - 1 - \Phi}$$

EQUATION 8 – GASSMANN - DRY ROCK FRAME BULK MODULUS CALCULATION

To calculate the dry rock frame's bulk modulus, the following parameters of the rock are required: the bulk modulus of the mineral matrix, porosity, and the bulk modulus of the pore filling fluid. To calculate the bulk modulus of the mineral matrix we can use the Voight-Reuss-Hill method (Smith et al., 2003):

$$K_o = \frac{1}{2}((F_1K_1 + F_2K_2) + ((\frac{F_1}{K_1} + \frac{F_2}{K_2})^{-1})$$

EQUATION 9 - VOIGHT-REUSS-HILL.

where F_n is the mineral fraction and K_n is mineral bulk modulus of the mineral. The above implementation accounts for a two-mineral system. The gamma-ray log was used to calculate shale volume, and the non-shale volume assumed to represent the quartz volume to assume a 2-mineral system of quartz and clay. Shale volume was calculated as follows;

$$v_{sh} = \frac{GR - GR_{Matrix}}{GR_{Shale} - GR_{matrix}}$$

EQUATION 10 – VOLUME SHALE

While the investigated reservoirs are more complex than a 2-mineral system, the constitute minerals have a bulk modulus of similar orders of magnitude. The similarity allows the use of a mixing law, which provides sufficient accuracy for the Gassmann equation. This is due to the bulk modulus of the mineral matrix only having a minor effect on the bulk modulus of the whole rock (Darling, 2005).

Porosity can be derived from well-log data; in this study we use the neutron-density methodology (Kennedy, 2015);

$$\Phi_\rho = \frac{\rho_{matrix} - \rho_{Bulk}}{\rho_{matrix} - \rho_{fluid}}$$

EQUATION 11 – DENSITY POROSITY

The bulk modulus of the fluid and ρ_{fl}, the bulk density of the fluid, can be derived for a single fluid or a fluid mixture. Either can be calculated via;

$$K_{fl} = [\frac{S_w}{K_w} + \frac{(1 - S_w)}{K_{fn}}]^{-1}$$

EQUATION 12 – BULK MODULUS OF FLUID MIXTURE

and;

$$\rho_{fl} = S_w * \rho_w + (1 - S_w)\rho_{fn}$$

EQUATION 13 – DENSITY OF FLUID MIXTURE

Once the bulk modulus of the pore filling fluid mixture has been determined, the bulk modulus of the mineral rock frame can be derived. With all constituent parts of the Gassmann equation established, the new elastic properties of the fluid-substituted rock can be calculated.

Along with the new bulk modulus of the fluid-substituted rock having, the bulk density of the rock with the substituted fluids can be calculated with;

$$\rho_{\mathrm{new}} = \rho_{\mathrm{matrix}} * (1 - \Phi) + (\rho_{\mathrm{fl}} * \Phi)$$

EQUATION 14 – DENSITY OF FLUID SUBSTITUTED ROCK

Once the new bulk modulus and bulk density of the rock have been calculated, the new compressional and shear velocities of the rock can be calculated by rearranging the equations for bulk modulus and G, the shear modulus. Note that the shear modulus of the rock remains unchanged despite fluid substitution;

$$\mathrm{Vp} = \sqrt{\frac{\mathrm{K} + \frac{4}{3}\mathrm{G}}{\rho_{\mathrm{bulk}}}}$$

EQUATION 15 – VELOCITY COMPRESSIONAL FROM BULK AND SHEAR MODULUS

$$\mathrm{G} = \rho_{\mathrm{bulk}} * \mathrm{Vs}^2$$

EQUATION 16 – SHEAR MODULUS

The equations used do not account for the carbon dioxide or hydrogen having been absorbed by residual water at non-end member water saturations. Our methodology also does not account for pore pressure changes, which can have effects on seismic responses (Bahmaei and Hosseini, 2020). We assume a uniform heterogeneous matrix and uniform liquid pathways. We assume the stored fluid (carbon dioxide or hydrogen) is fills the pore space as a fluid and do not consider the precipitation of any fluid into the mineral phase, or dissolution into brine.

1.4.3 Determining net reservoir

Reservoir cut-offs were used to define reservoir intervals within wells. Shale volume (Vshale), porosity and bulk density were the chosen factors in determining which areas of the reservoir were suitable (Table 2). A shale volume value of 30% was selected as the cutoff volume. The bulk density values were chosen, as outside these ranges typically consisted of either A) interbeds of low-density evaporites such as halite or B) interbeds of high-density evaporites such as anhydrites or carbonates. A minimum porosity of 5% was chosen.

1.4.4 Stochastic modelling

A stochastic approach to implementing the Gassmann equations was adopted to quantify the impact of the uncertainty in reservoir and fluid properties. This approach was implemented using Python 3.10.13. In uncertainty quantification Monte Carlo methods have become common place as they allow for the examination of a wide parameter space, can incorporate different distributions for different parameters and outputs are probabilistic with a quantification of uncertainties (Zhang, 2020). In the method developed the input properties are derived from well logs. The elastic property inputs of the Gassmann equations were defined as distributions derived from well data. The elastic properties of porous material can be correlated (Appendix 1); hence, a multi-variate distribution was derived from the properties (Castagna et al., 1993). Distributions were determined for defined porosity intervals (Table 3). For a valid distribution to be defined, a minimum of 25 data points was required, ensuring the shape of the distribution to be suitably characterised, and for the avoidance of edge cases. The compressional velocity, shear velocity, porosity, bulk modulus and shale volume were the required parameters to be derived from porosity-separated distributions for the Gassmann equations. For each porosity of each formation investigated (Table 3) there were 1,500 iterations of the model run. Our 'computationally low' methodology takes ≈15 seconds to compute 1500 iterations of the Gassmann equations. Multi-variate distributions were also created for the seal paired with the reservoir intervals. The distribution for these was used within the AVO analysis, so the well data was used to derive distributions for shear/compressional velocity and bulk density of the seals. Alongside stochastic modelling we use the UQ(Py)Lab package for Python to undertake a sensitivity analysis using the Solbol methods (Soboĺ, 1993; Marelli and Sudret, 2014). The output chosen to investigate the sensitivity of the Gassmann equation was the new acoustic impedance of the fluid-substituted rock. The use of sensitivity modelling allows for understanding which parameters within the Gassmann equation have the most significant effect on the resultant acoustic impedance.

1.4.4.1 Validation of parameters for stochastic modelling

While compressional and shear velocity and, bulk density, can be directly derived from the data taken from the well logs, other parameters, notably porosity and bulk modulus of the mineral matrix, must be calculated using transforms that relate to theoretical relationships. Calculated porosity values for the Bunter Sandstone were checked against those from measured core plug values (Appendix 11). 10 porosity measurements from core were randomly sampled and compared with the calculate porosity at the same depth. The average difference between the measured values and calculated values was found to be 11% (e.g. 20% vs 22.2% porosity), which was determined to be reasonable.

To validate the calculated values for the mineral matrix bulk modulus, due to lack of other independent data from which to compare, we used literature to determine typical mineral percentages for the matrix and check against our shale volume and quartz volume estimates (Howard et al., 2008; Scorgie et al., 2021; Qin et al., 2022). We assume a 2-mineral system, as the only other main mineral within the system (apart from clays) is likely to be feldspar. The average value for feldspars' bulk modulus is similar to that of quartz (37.5 vs 37), thus for this use it was deemed suitable (Smith et al., 2003). We do not attempt to verify calculated bulk modulus of the mineral matrix, K_o, as even if exact values for the mineral matrix components were available, there are high levels of variability between the two parameters, as shown by Qin et al. (2022).

1.4.5 Seismic responses

Once the new elastic properties are calculated, the seismic response can be calculated. The new reservoir elastic properties and associated seismic response of the fluid-substituted reservoirs were calculated for water saturations from 100% to 0% in 10% increments. We investigated the impact of hydrogen and carbon dioxide. We model methane (natural gas) as a reference case.

1.4.5.1 Wedge modelling

Wedge models were created to model the seismic response at geological interfaces. The wedge models were produced in Python using parts of the PySeisTuned 2.0 code base (Dowdell, 2020). Two wedge models were created for each reservoir–seal pair investigated: reservoir-reservoir interfaces and seal–reservoir interfaces. The wedge models used simple three-layer geological models, which included an overburden, the reservoir wedge and the underburden. The rock properties used in the wedge models were derived from the deterministic fluid substitution scenarios for the reservoir, and well logs for the original reservoir and seal properties. The acoustic impedance was calculated for each wedge section and, subsequently, the reflection coefficient at the wedge interfaces. A ricker wavelet with a frequency analogous to the seismic data that covers the area of the well data was used (Bunter formation = 35Hz, Helsby = 40Hz, Leman = 32 Hz). The wavelet was convolved with the reflection coefficient to generate a synthetic wedge model. The wedge models use the SEG standard polarity, where a negative reflection coefficient event shows a negative reflection event.

1.4.5.2 AVO Responses

Amplitude versus offset (AVO) analysis examines the change in reflection and transmission coefficient of an incident P-wave (compressional wave, V_p) as a function of the angle of incidence (Chopra and Castagna, 2014). For interface modelling and calculating the expected amplitude versus the offset of the seismic wave (AVO), the Zoeppritz's equations was used (Zoeppritz, 1919);

$$\begin{bmatrix} \cos\theta_{p1} & -\sin\theta_{s1} & \cos\theta_{p2} & \sin\theta_{s2} \\ \sin\theta_{p1} & \cos\theta_{s1} & -\sin\theta_{p2} & \cos\theta_{s2} \\ Z_1\cos2\theta_{s1} & -W_1\sin2\theta_{s1} & -Z_2\cos2\theta_{s2} & -W_2\sin2\theta_{s2} \\ \frac{V_{s1}}{V_{p1}}W_1\sin2\theta_{p1} & W_1\cos2\theta_{s1} & \frac{V_{s2}}{V_{p2}}W_2\sin2\theta_{p2} & -W_2\cos2\theta_{s2} \end{bmatrix} \begin{bmatrix} R_p \\ R_s \\ T_p \\ T_s \end{bmatrix} = \begin{bmatrix} \cos\theta_{p1} \\ -\sin\theta_{p1} \\ -Z_1\cos2\theta_{s1} \\ \frac{V_{s1}}{V_{p1}}W_1\sin2\theta_{p1} \end{bmatrix}$$

EQUATION 17 –THE ZOEPPRITZ (1919) EQUATIONS

The Zoeppritzs equations allow for the calculation of the reflected p-wave response at a geological interface with a set angle of incidence. For the application of the AVO equations to our data, we used the Python module Bruges by Agile-Scientific (2022) which is based on the methodology described by Dvorkin et al. (2014). Each generated value from the stochastic analysis of the reservoir response analysis (Section 1.4.4, 1500 values total) was used as an input into the Zoeppritz equations. Using the previously generated values, allowed for the range in possible AVO response values to be captured. Two separate geophysical responses were modelled, reservoir – reservoir contacts (water saturation 100% and water saturation

0%) and seal – reservoir contacts. The seal parameters used within the Zoeppritz were generated from the seal multi-variate distributions (Section 1.4.4).

1.4.5.3 Timeshift analysis

As fluids within the pore-space affect the compressional and shear velocity properties of a rock, they affect the travel time of seismic waves through the media and modify the recorded responses in the seismic surveys (Dvorkin et al., 2014). Time-shift analysis involves identifying the time variation between two seismic traces in the same location from different acquisitions. These are typically taken pre-fluid injection/withdrawal (baseline) and after fluid injection or withdrawal (monitor) (MacBeth et al., 2020). Two methods were used to investigate the time shifts caused by fluid substitution, 1) Using a baseline and monitor seismic trace generated from well data to measure the timeshift on actual geological data and, 2) From stochastically generated compressional velocities for baseline and monitor reservoir values to calculate Δt over various distances and water saturations.

$$\Delta t = z\left(\frac{1}{v'} - \frac{1}{v}\right)$$

EQUATION 18 TIME-SHIFT ESTIMATION FROM MACBETH ET AL. (2018)

1.5 Data

From the three chosen reservoir-seal pairs, the wells were selected based on the availability of data. We prioritised wells that had bulk density, shear slowness, compressional slowness, gamma ray and neutron porosity logs across reservoir intervals. This requirement for shear slowness data limited well selection as it is not commonly acquired. The stratigraphic intervals within the well logs were identified using the completion logs, which were available for each well through the North Sea Transition Authority's National Data Repository (https://ndr.nstauthority.co.uk/). For the wells used within this study, please view the appendix.

Due to limited shear slowness data availability in wells from the Helsby and Bunter Sandstone Formations, the parameter distributions are derived from a single well, whereas, for the Leman, more wells had the required logs available, which allowed for distributions to be derived from multiple wells. As the modelling of the Bunter Sandstone used a single well it effectively investigates the vertical heterogeneity and uncertainty, while for the Leman

Sandstone that availability of data means the modelling effectively investigates the lateral and vertical heterogeneity.

1.6 Results

1.6.1 Reservoir Responses

1.6.1.1 Response to different fluids (Deterministic)

The change in water saturation from 100% – 80% for all fluids and reservoirs shows a sharp initial drop in compressional velocity, however, after this initial drop, compressional velocity begins to increase (Figure 3). Hydrogen and methane in all reservoirs increase the compressional velocity beyond the initial value at between 40% - 20% water saturation. However, after an initial drop the compressional velocity due to carbon dioxide increases at a proportionally slower rate than that of hydrogen and methane, in each scenario. The compressional velocity for each reservoir never increases over the initial value for carbon dioxide.

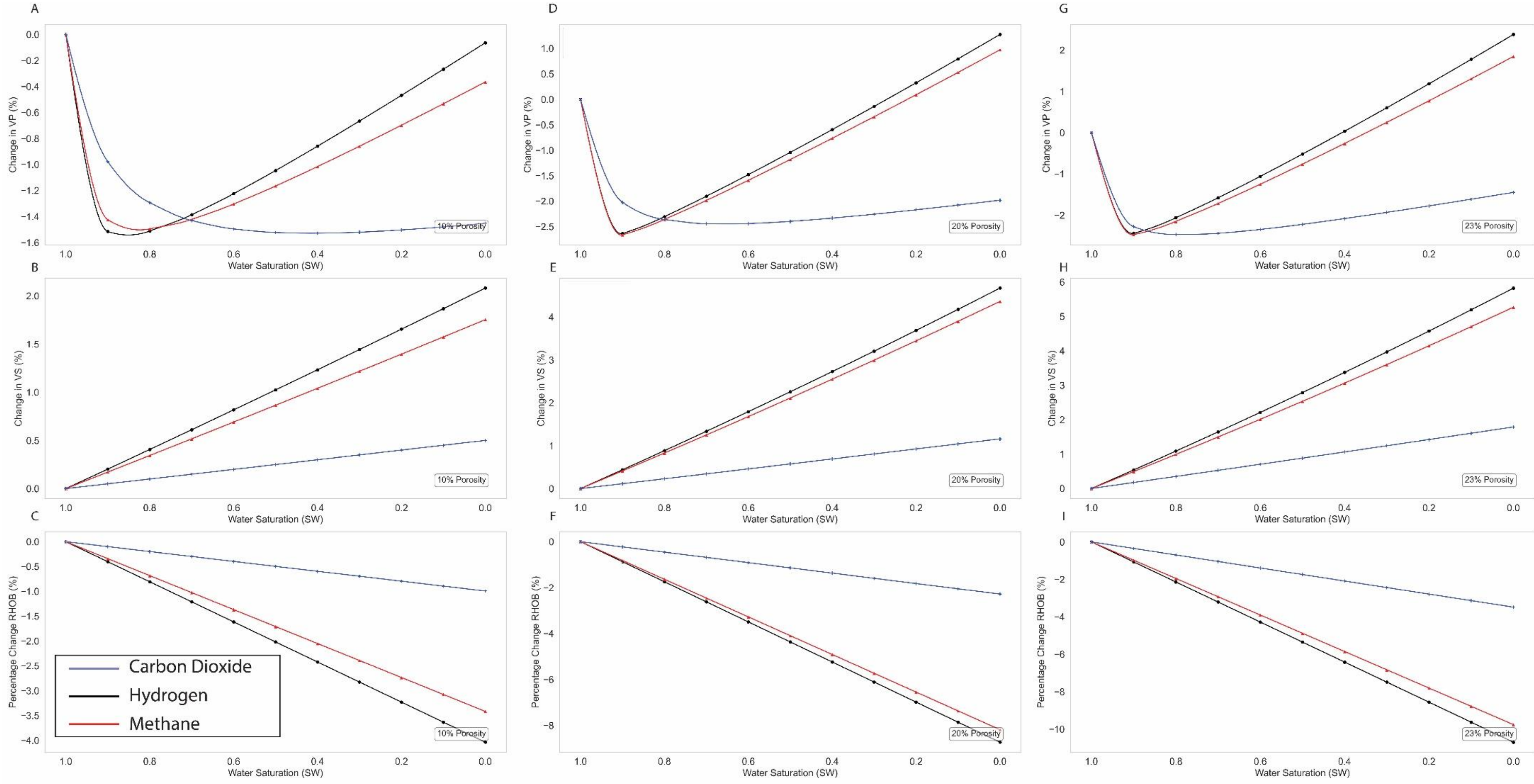

FIGURE 3 DETERMINISTIC ELASTIC RESPONSES OF THE LEMAN (A-C), BUNTER (D-F), HELSBY (G-I). GRAPHS A,D,G SHOW % CHANGE IN COMPRESSION VELOCITY, B,E,H SHOW % CHANGE IN SHEAR VELOCITY AND C,F,H SHOW % CHANGE IN BULK DENSITY

The change in shear velocity for all reservoir fluid combinations is a positive linear increase (Figure 3). There are differences amongst the fluids however. Hydrogen in all scenarios has the greatest increase, with methane showing similar increases. Carbon dioxide has the lowest increase in shear velocity overall for all scenarios. As the porosity of the reservoir has increased so has the % increase of shear velocity (Figure 3).

Change in bulk density is a negative linear trend for all scenarios. This occurs as the substituted fluids all have densities lower than water (Figure 3). Substitution of carbon dioxide into the pore space causes a smaller percentage change to the bulk density than hydrogen, due densities at reservoir conditions. The higher porosity reservoir undergoes the highest percentage change to bulk density because there is more pore space for the less dense fluids into which they can be substituted.

The sensitivity analysis of the Gassmann equation for calculating acoustic impedance shows that it is most sensitive to a change in compressional velocity, with a first-order index value of 78% and a total Sobol index of 53% (Figure 4). Moderate sensitivity to both porosity and density is indicated, with first order results being 20.7 % and 20.4 % and total order indexes being 4.9 % and 5.5 % respectively. The equation is not sensitive to shear velocity or the mineral matrix composition.

1.6.1.2 Stochastic analysis of geophysical responses

We concentrate on describing the results of the fluid substitution at 20% water saturation, as this is likely the near maximum value possible for subsurface storage sites (Yan et al., 2018). The Leman data set was split into seven porosity groups with a 2% porosity interval from 7% to 19% (Table 3). Increasing the proportion of hydrogen results in a greater acoustic impedance change than for the equivalent carbon dioxide at each porosity interval. The largest change in acoustic impedance for 20% water saturation for both hydrogen and carbon dioxide occurred at 19% porosity, being -12.7% and -9.2% respectively (Figure 5). Hydrogen has a much sharper initial decrease in acoustic impedance compared with carbon dioxide (Figure 5).

For the Bunter Sandstone, the p50 results, hydrogen is shown to modify the acoustic impedance a greater amount than carbon dioxide, at 27% porosity and 20% water saturation. The effect change for these reservoir parameters on acoustic impedance for hydrogen is -9.8%

and for carbon dioxide it is -6.7%. The trend is the same as those in the deterministic reservoir responses (Figure 6) with hydrogen having a sudden drop at 90% water saturation and then a relatively continuous linear decrease, whereas carbon dioxide has a more pronounced curve to its trend in decreasing acoustic impedance (Figure 6). The minimum response for hydrogen and carbon dioxide in the p50 values is both at the lowest porosity, 19%, where at 20% water saturation, hydrogen has an acoustic impedance change of -6.2% and carbon dioxide has a negative change of -4.2%.

The results for the Helsby Sandstone follow the same trends as the Bunter data, with higher porosities having a larger effect on acoustic impedance and hydrogen also having a larger effect. At 26% porosity and 20% water saturation, hydrogen fluid substituted sample showed a change in acoustic impedance of -10.4%, while carbon dioxide was -6.5%. At the lowest porosity, 14%, the change in acoustic impendence at 20% water saturation was -2.8% for hydrogen and -1% for carbon dioxide.

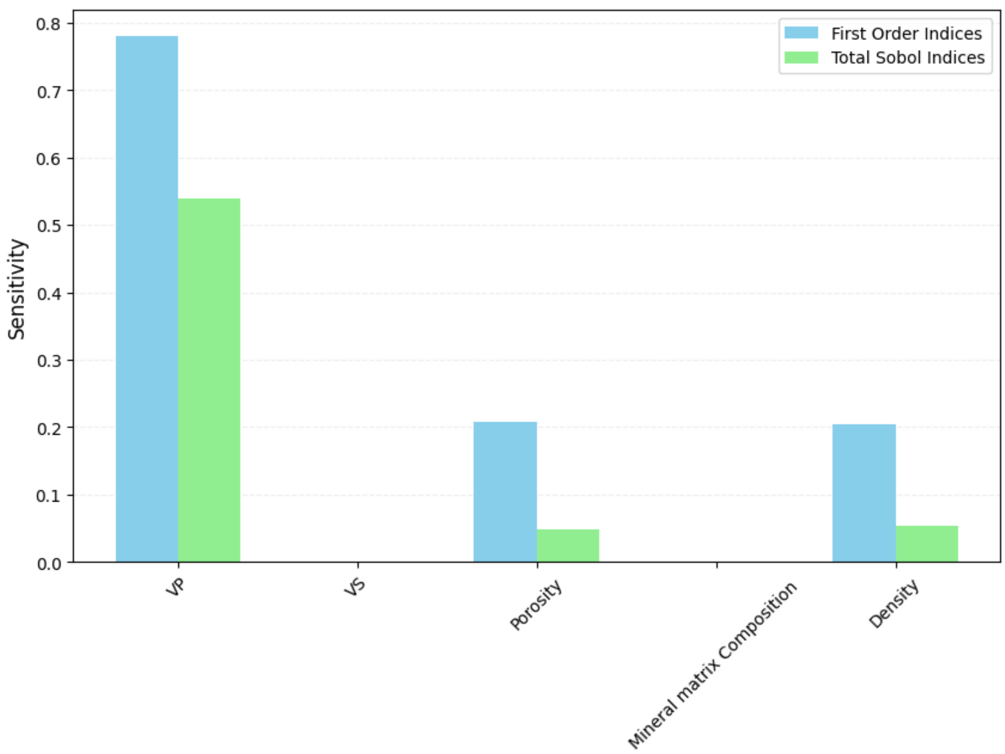

FIGURE 4 SOBOL SENSITIVITY ANALYSIS RESULTS FOR THE PARAMETER INPUTS DERIVED FROM WELL LOG DATA ON THE GASSMANN EQUATION FOR THE COMPUTATION OF THE ACOUSTIC IMPEDANCE.

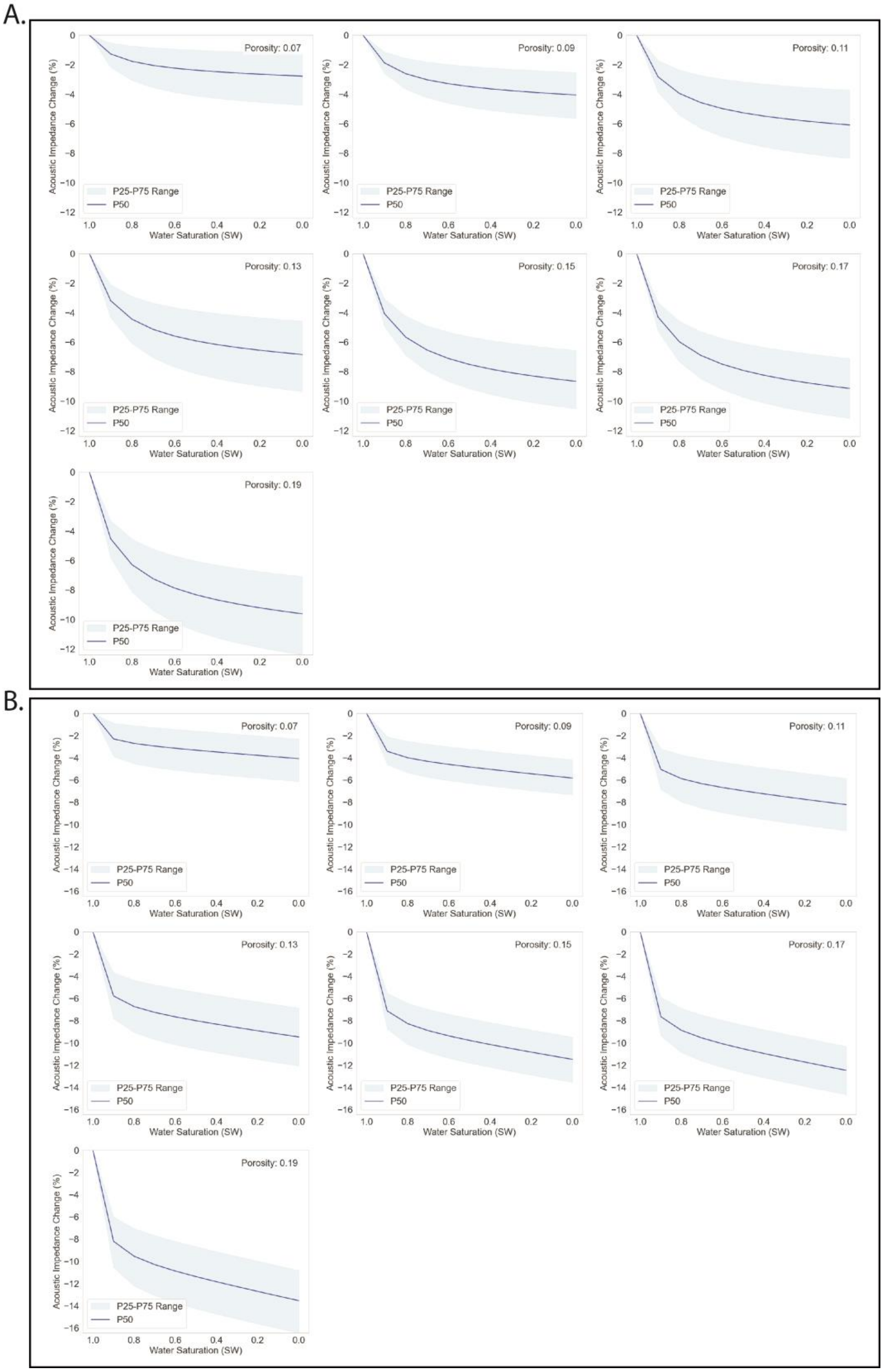

FIGURE 5 LEMAN STOCHASTIC ACOUSTIC IMPEDANCE MODELS FOR VARYING POROSITY VALUES AFTER FLUID SUBSTITUTION FOR FLUIDS. A) CARBON DIOXIDE, B) HYDROGEN

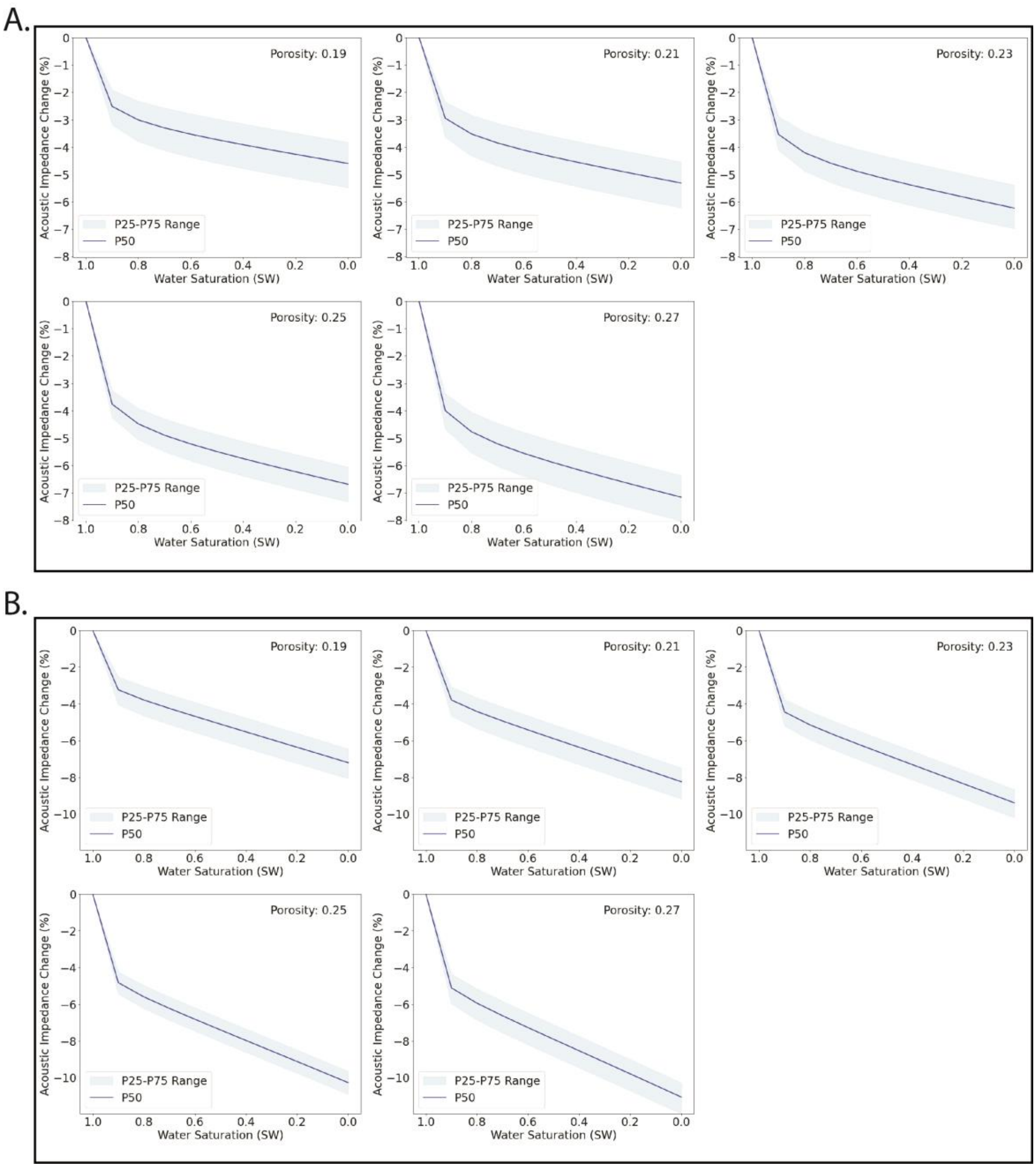

Figure 6 Bunter stochastic acoustic impedance models for varying porosity values after fluid substitution for fluids. A) Carbon dioxide, B) Hydrogen

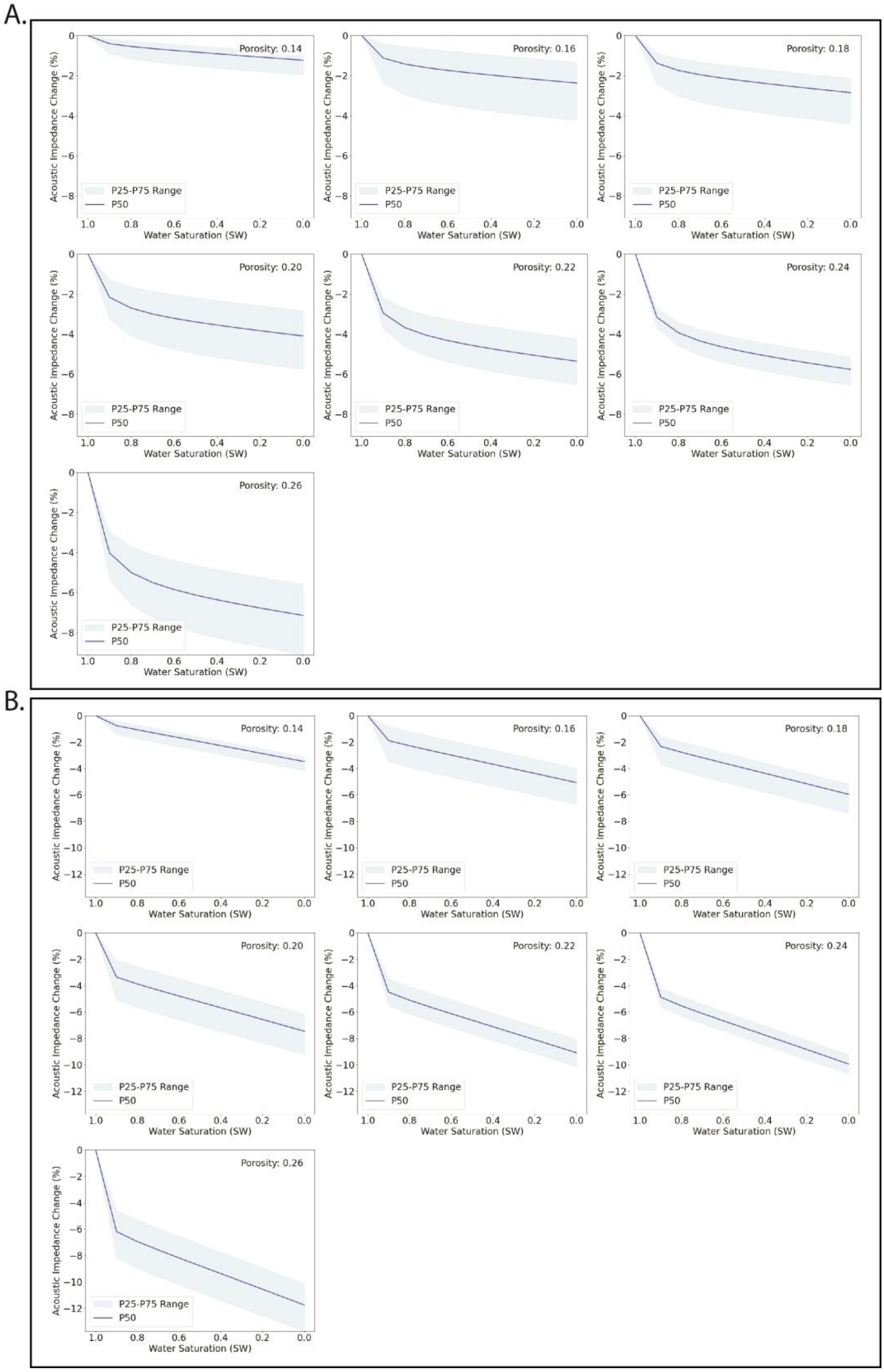

FIGURE 7 HELSBY STOCHASTIC ACOUSTIC IMPEDANCE MODELS FOR VARYING POROSITY VALUES AFTER FLUID SUBSTITUTION FOR FLUIDS. A) CARBON DIOXIDE, B) HYDROGEN

1.6.2 AVO responses

Figure 8 shows the modelled AVO responses for the reservoir–reservoir and reservoir–seal interface for the Leman Sandstone at 7%, 13% and 19% (other values in Appendix 12 - 17). The reservoir-reservoir interface shows small decreases in the amplitude for typical changes in the recorded reflection offsets from seismic data, however these small decreases do result in large percentage changes, for example at 19% porosity, the amplitude at 5° is -0.072 and at 45° the amplitude is -0.097, a change of -35.6%. More notable differences in amplitude occur at offset angles which are greater than that which would typically be recorded with a conventional seismic survey (45°+), and this is common for all porosities. However, for the reservoir–seal interface there are noticeable differences to the amplitude at typical survey offsets for all porosities. The largest change as offset increased was for the 19% porosity seal-reservoir interface, where from 5° (near stack) to 45° (ultra far stack) there was a relative amplitude change of +0.14.

As the Bunter Sandstone has two possible seals within the Southern North Sea, halite and claystone, both interface lithologies were modelled for their AVO response (Figure 9). For the reservoir-reservoir interface AVO analysis, both carbon dioxide and hydrogen results show moderate to minor differences in amplitude with an increase in offset from the near stack to the ultra-far stack with a difference of 17.0 - 18.7% and 5.9 – 4.7% (7 – 19% porosities) respectively. The amplitude difference for the carbon dioxide filled reservoir is smaller with an increasing offset, with the most noticeable change occurring at offsets of +50° where amplitudes decrease rapidly. The inverse is true for hydrogen, where there is a minor increase in amplitude for all porosities throughout increasing offset, with the most notable changes being large increases again after +50°. The evaporite seal–reservoir interface shows very similar results for both hydrogen and carbon dioxide (Figure 6). Minor amplitude differences are apparent; however these do not impact the trend of the amplitude differences. The claystone seal model again has similar results for both carbon dioxide and hydrogen, with only minor amplitude differences up until reaching the ultra-far offset values. At the ultra-far offset values, the lower porosities amplitude falls, whereas the higher porosity values increase slightly.

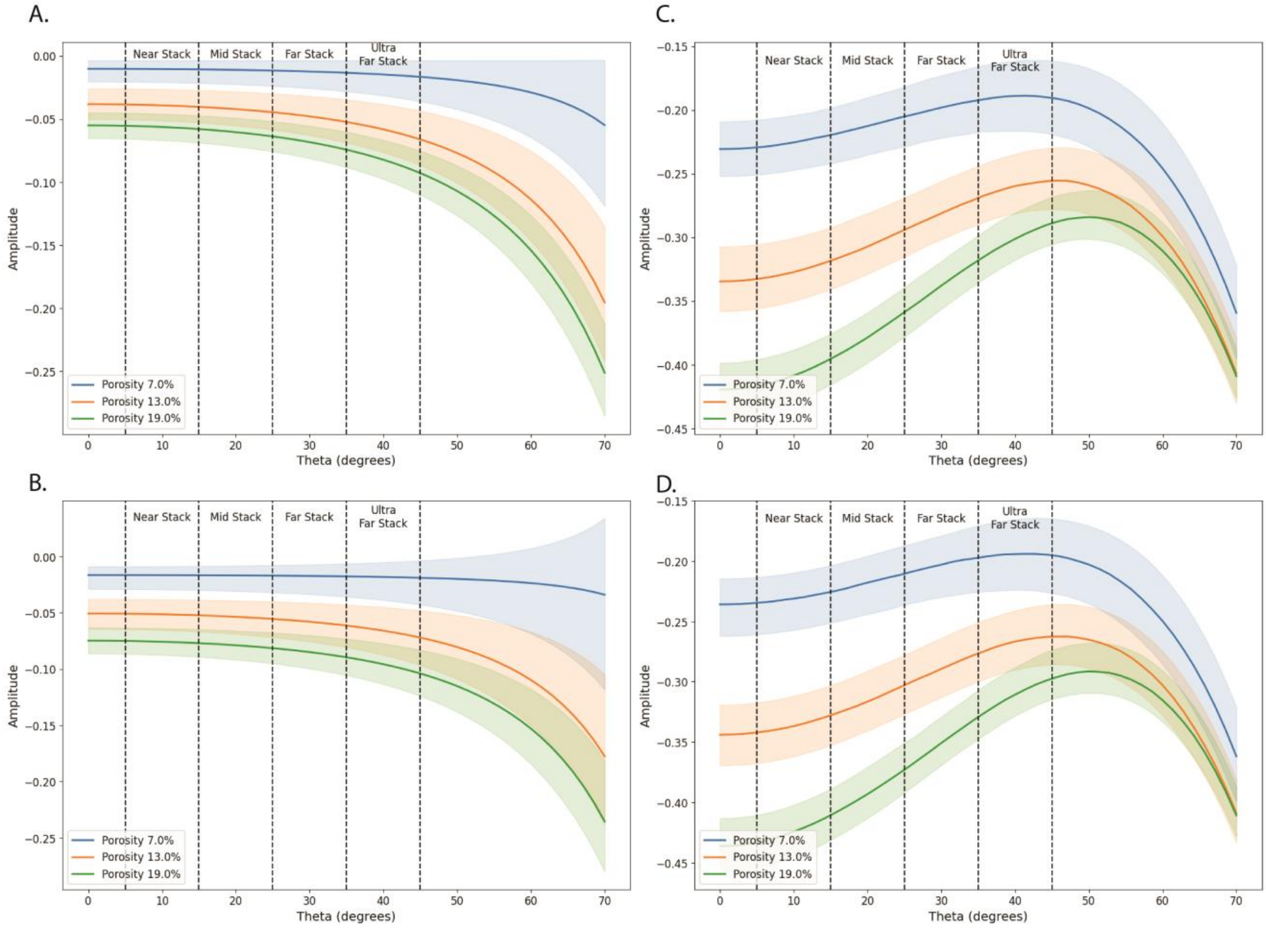

Figure 8 Leman amplitude versus offset for reservoir-reservoir interface for (A) Carbon Dioxide and (B) Hydrogen. Seal-reservoir interface for (C) Carbon Dioxide and (D) Hydrogen

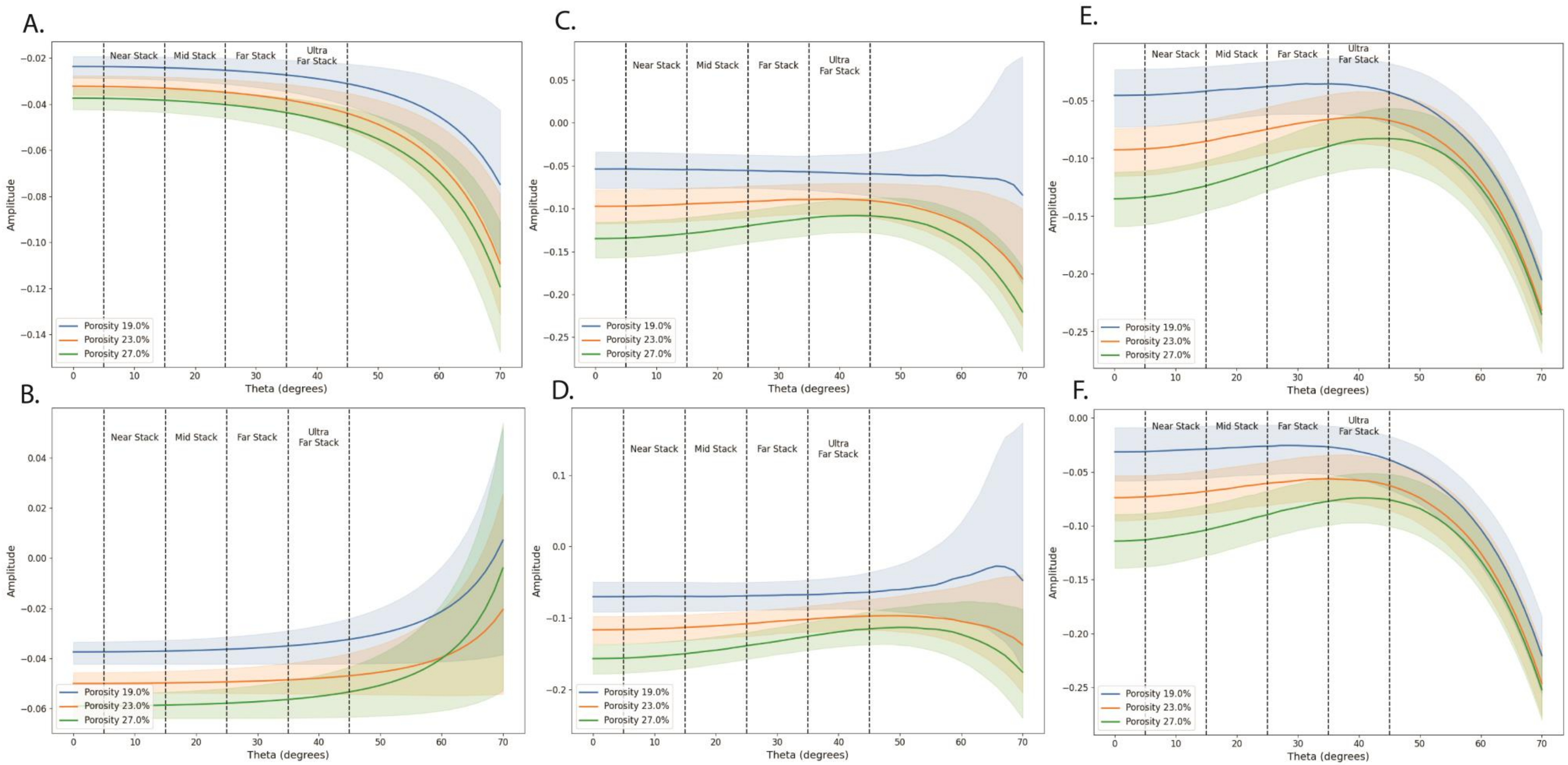

FIGURE 9 BUNTER AMPLITUDE VERSUS OFFSET FOR RESERVOIR-RESERVOIR INTERFACE FOR (A) CARBON DIOXIDE AND (B) HYDROGEN. SEAL-RESERVOIR (EVAPORITE) INTERFACE FOR (C) CARBON DIOXIDE AND (D) HYDROGEN. SEAL-RESERVOIR - (CLAYSTONE) INTERFACE FOR (E) CARBON DIOXIDE AND (F) HYDROGEN.

The results for the Helsby Sandstone show a minor difference of decreased amplitude for the reservoir–reservoir interface for carbon dioxide and a minor increase for hydrogen in the typically recorded offset ranges (Figure 10). At large offsets (+45°), the carbon dioxide reservoir – reservoir interface shows a decreased value for amplitude for every porosity except for the 14% porosity values, which increase. Hydrogen results show all amplitudes increase at these offsets at greater than 45°, with the lowest porosity, 14%, showing the greatest increase. For the carbon dioxide seal-reservoir interface, an increase in amplitude from low to high offsets is observed for all porosities. This increase in relative amplitude peaks in the range of 50°- 60°, after which it falls rapidly. For hydrogen the results for higher porosities are like that of the carbon dioxide, however, for the lower porosities, notably 14%, a gradual decrease in relative amplitude occurs, with a greater drop off offsets of 65°+ (Figure. 8).

1.6.3 Interface modelling

Reservoir-seal and reservoir-reservoir interfaces were modelled for the Bunter Sandstone for hydrogen and carbon dioxide (Figure 11). All models show initial constructive interference at wedge thicknesses <10 ms. All models show the onset tuning to occur at a wedge thickness of 14 ms, after which constructive interference occurs. The reservoir-seal interfaces both have onset tuning thickness of 28 ms, while the reservoir-reservoir interfaces onset tuning thickness is 29 ms. The interface wedges for hydrogen (Figure 11 E,F) show higher amplitude values than those for carbon dioxide (Figure 11 C,D).

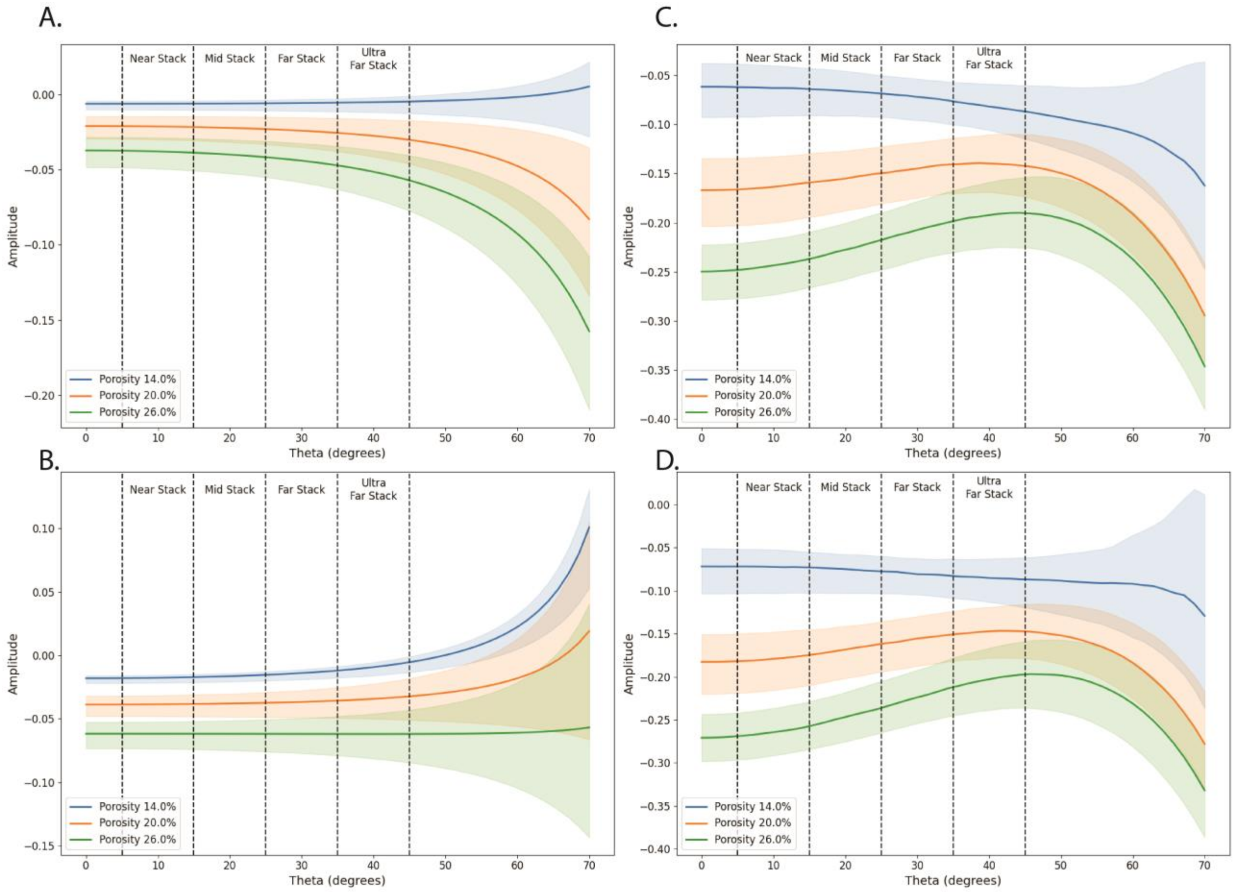

FIGURE 10 HELSBY AMPLITUDE VERSUS OFFSET FOR INTERFACE FOR (A) CARBON DIOXIDE AND (B) HYDROGEN. SEAL-RESERVOIR INTERFACE FOR (C) CARBON DIOXIDE AND (D) HYDROGEN

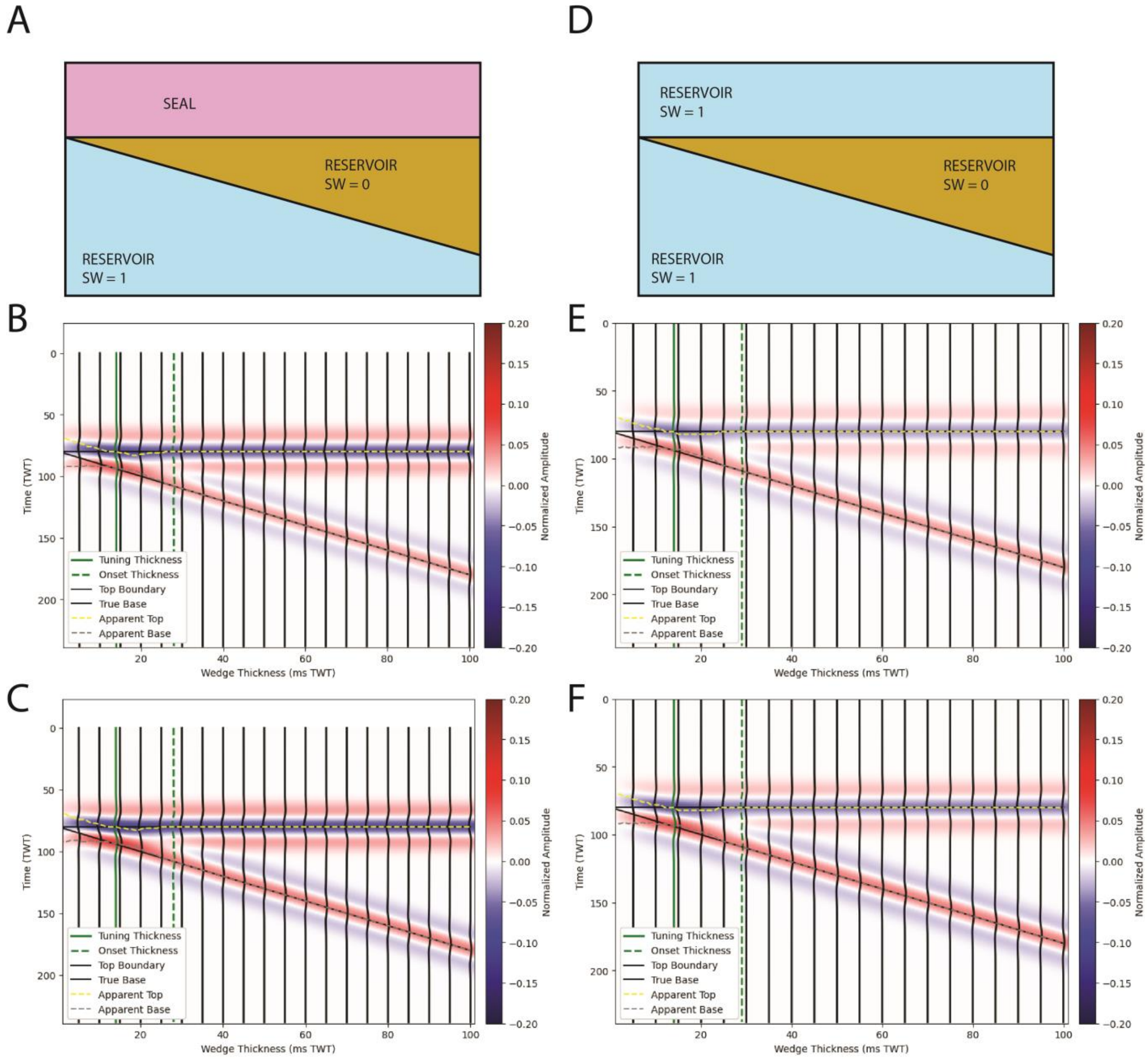

Figure 11 Interface seismic wedge models. A) 2D block diagram of geology simulated for B and C. B) reservoir saturated with Carbon Dioxide (C) Hydrogen. D) Block diagram of simulated geology for E and F. E) Reservoir saturated with Carbon Dioxide, (F) Hydrogen. Frequency used for wavelet is 35Hz

1.6.4 Time Shift

Synthetic seismic traces were calculated for the Bunter Sandstone from well log data (well 42/25-d3, 130 m section of reservoir). Traces were made for pre and post-fluid-substitution (20% water saturation) of carbon dioxide to act as baseline and monitor seismic traces. Figure 12 shows the monitor, baseline, and an overlay for the synthetic seismic well traces from the Bunter Sandstone well for carbon dioxide. A positive timeshift for the monitor initiates at the top of the reservoir when brine is replaced with carbon dioxide, with a shift in seismic traces (Figure 12). The difference in TWT at the bottom of the reservoir is 0.877 ms over the reservoir interval of 130 m. Time shifts for the Bunter Sandstone were calculated using the velocity values generated from the gassmann equations during the stochastic fluid substitution analysis in section 5.1.2 (equation 16).

Initial low water saturations (0.7,0.8) show the greatest timeshift over any set unit thickness, with the p50 value at 0.7 having a timeshift of 2.46 ms for 250 m (Figure 12). This aligns with the values seen in section 4.1.2 where large decreases in Vp are initially observed at relatively high-water saturation values (Figure 3). Extrapolating values to match the reservoir thickness in Figure 12, at 0% water saturation and a 130 m reservoir, the calculated timeshifts are 0.93 ms for the p50, 0.64 ms for the p25 and 1.11 ms for the p75. This locates the calculated value from the log derived timeshift (0.72 ms) within the range of provided values.

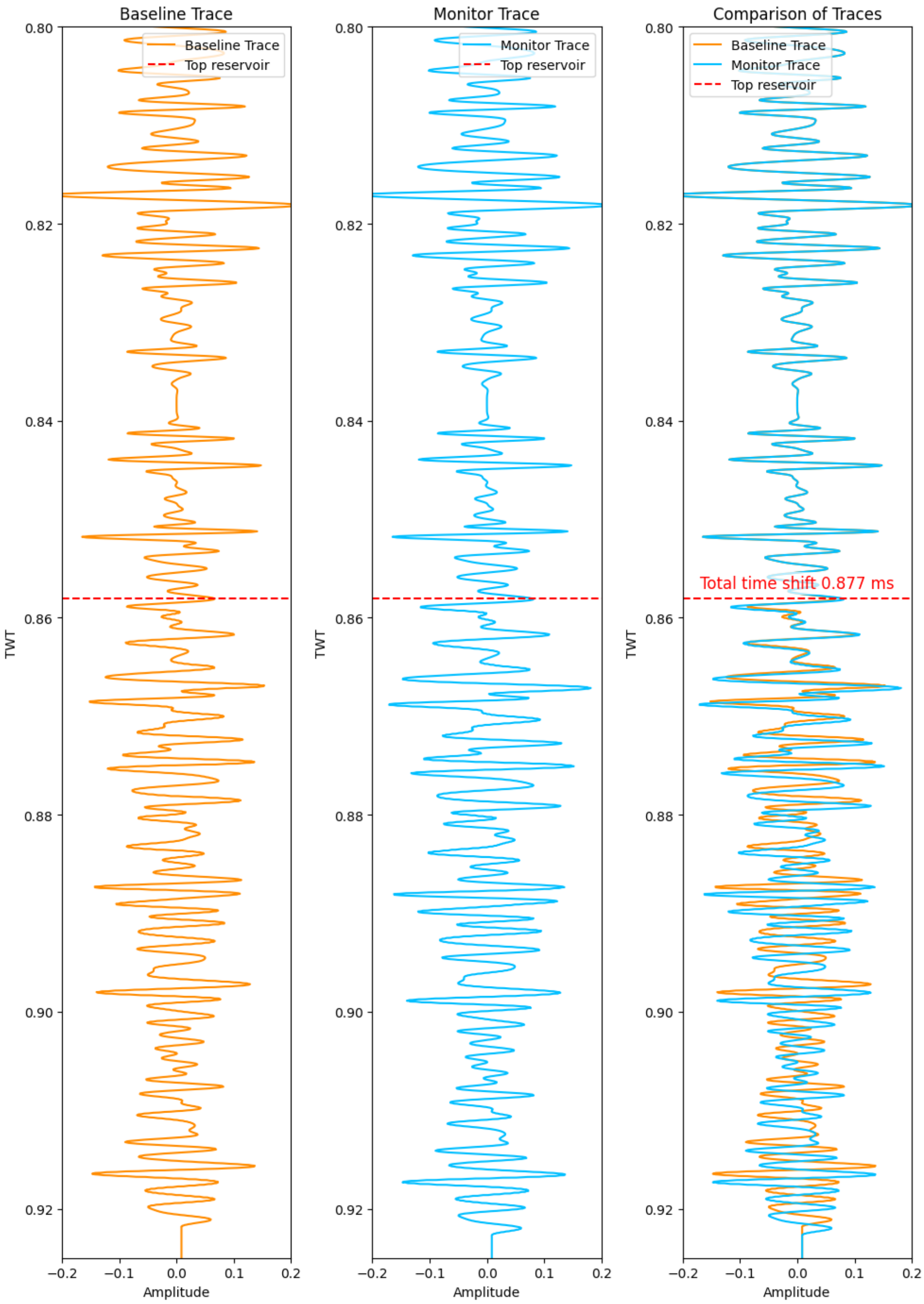

Figure 12 Bunter reservoir interval from well 42/25-d3 (Red line = top of reservoir). (A) Baseline synthetic seismic log, (B) Monitor synthetic seismic log after Gassmann fluid substitution 100% carbon dioxide saturation. (C) A + B overlain one another for visible timeshift comparison

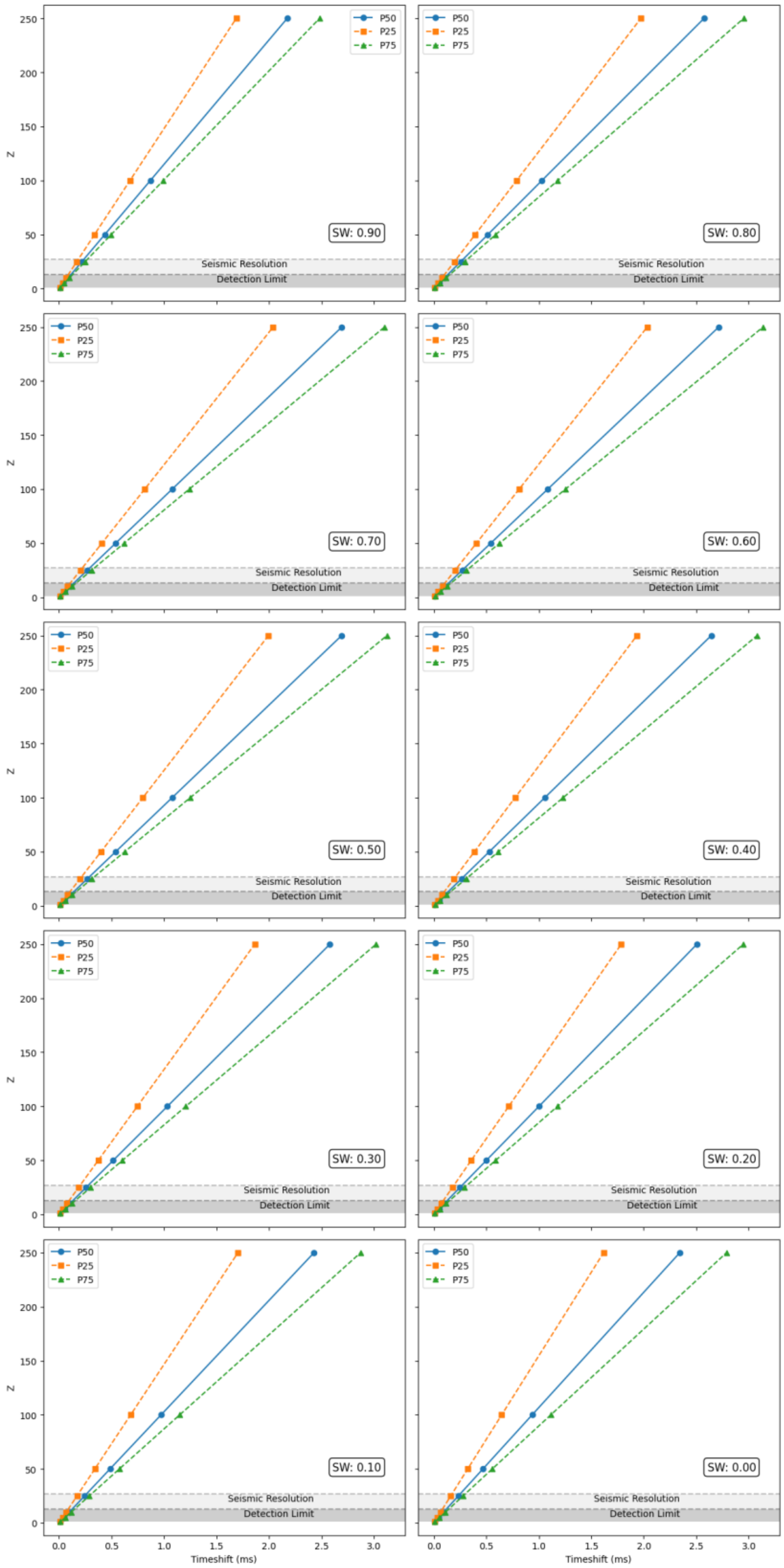

FIGURE 13 SYNTHETIC TIMESHIFT MODELS FOR THE BUNTER SANDSTONE. 90% – 0% WATER SATURATION IS MODELLED FOR A THICKNESS OF 0 – 250. P25, P50 AND P75 VALUES ARE INCLUDED. THE RESOLUTION (27 M) AND DETECTION LIMIT (13 M) OF THE SEISMIC FOR THIS WELL AND DEPTH ARE INCLUDED.

1.7 Discussion

1.7.1 Results

The results from the stochastic modelling of the storage reservoirs are expected to exhibit a decrease in acoustic impedance when brine is replaced by either carbon dioxide or hydrogen (Figure 5,7). For all reservoir intervals, higher porosities result in a greater change to acoustic impedance. Between the reservoir formations, for the same porosity, for example 19% porosity for the Leman and Bunter Formations, there are large differences to the change in acoustic impedance values, for the Leman, a p50 of 9.2% and for the Bunter a p50 of 4.2% at 20% water saturation (Figure 5,6).

The acoustic impedance results for the Bunter Sandstone have a narrower range for the p25 and p75 results compared with both the Leman and Helsby examples (Figure 6-8). The difference in ranges for outputs is likely the result of two factors. Firstly, the input data for both the Leman and Helsby multivariate distributions shows a much larger range of values, and a higher quantity of outliers present than compared with the Bunter values (Figure 14). The wider ranges of generated values from the multivariate distributions coincide with formation and porosity intervals with large p25 – 75 ranges for acoustic impedance results, for example the Leman 13% porosity and Helsby 22% porosity interval (Figure 5,6,14). Secondly, the increase in pore-fluid being substituted led to large ranges within the output results. Every output result for change in acoustic impedance shows a significantly lower range in output values for the initial 100% – 70 % water saturation, with saturations from 70% – 0% showing increased ranges for the p25 – p75 values. It is likely the increased variation in ranges for results shown for acoustic impedance is from a combination of these effects.

1.7.2 Comparison with published results

We discuss the results of our modelling with other published results for the same reservoir storage formations. Our results (Table 4) show different values to those given in reports on monitoring of the stratigraphy we investigated, notably to James et al. (2016b) for the Leman, to Green and Grammer (2016) for the Helsby and to BEIS (2021) for the Bunter Sandstone. Seismic monitoring is a valid technique to monitor migration pathways for carbon dioxide using change of acoustic impedance. However, the properties unique to the rock being monitored may mean that the change in elastic properties is below that of the detection limit of the seismic data. As a rule of thumb, an acoustic impedance contrast of 4% is required for a 4D seismic survey to detect the change in a feature (Lumley and Behrens, 1998). Table 4 shows that the predicted acoustic response from the Leman is well above this 4% boundary, however the Bunter is only just above this boundary and the Helsby is < 4% boundary. As the cited sources did not provide the parameters used within their workflow or the output models, direct comparisons with the results presented in this study are difficult. Had such data been given in a readily accessible data base more in-depth comparisons could have been concluded.

While changes in acoustic impedance values in seismic data can aid in the monitoring of subsurface fluid migration, utilising the changes to seismic amplitude with different seismic reflection offsets, utilising different qualities within the same dataset, may aid in further detecting the change in acoustic impedance and provide more informative results for carbon dioxide plume monitoring. For example, both the Leman and the Bunter Sandstone (Table 3,Figure 8,9) show larger % changes for the reflection coefficient and hence amplitude at the interface of reservoir – reservoir and seal – reservoir than the % increase when calculating just acoustic impedance change (Table 3).

The results of timeshift analysis also indicate notable variations in reflection two-way-time because of changes in fluid saturations (Figure 13). The plotted detection limit (13 m) and seismic resolution (27 m) show that at the detection limit, the resolvable timeshift values range from 0.09 ms to 0.11 ms, and for the seismic resolution, the timeshift values vary from 0.22 ms to 0.27 ms. Typical detection limits for timeshift values reported from separate monitor seismic surveys range from 0.1 ms – 2 ms in literature (MacBeth and Izadian, 2023). The calculated timeshift of 0.8 Sw is 0.77 ms for the Bunter Sandstone from well 42/25d-2 (Figure 12), and is therefore likely detectable on a monitor seismic survey. However, this timeshift occurs from a 130 m reservoir thickness interval, as such reservoir thickness below the suggested timeshift detection limit (13 m) may not be detectable in a monitor survey.

The relatively positive findings from our study, however, do not excuse the literature sources for failing to give quantifiable inputs and results for their fluid substitution modelling and analysis. If the cited sources are supportive of seismic monitoring and such methods are proposed for large-scale infrastructure projects, there should be stringent evidence supplied in a repeatable and reliable manner, as shown in this study.

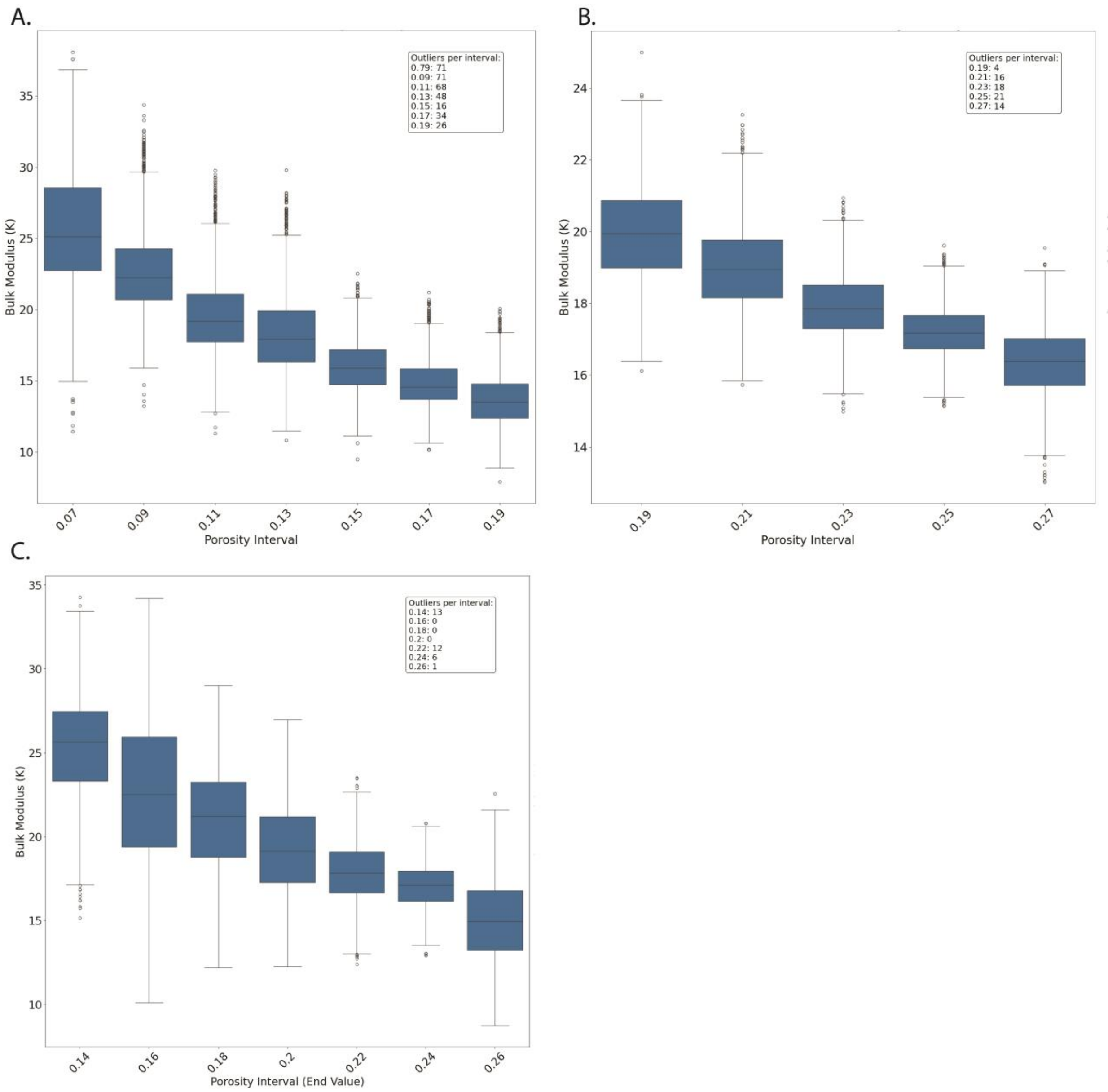

FIGURE 14 BOX PLOTS BULK MODULUS FOR POROSITY INTERVALS FROM MULTIVARIATE DISTRIBUTIONS FOR A) LEMAN, B) BUNTER, C) HELSBY

The reproducibility and reliability of methods for subsurface monitoring is important for subsurface infrastructure projects, as it allows for evaluation of results to be more efficient and undertaken reliably, strengthening evidence for proposed projects (Steventon et al., 2022). However, a common theme regarding site specific subsurface storage, is the lack of data supplied to allow for results to be seen as both reproducible (same data same methodology), or reliable (same data different methodology). While best efforts were made to replicate the results of those published in literature (Table 4), this was not possible (Green and Grammer, 2016; James et al., 2016a, 2016b; BEIS, 2021). While we cannot comment on which results are more accurate, we can provide all data and the methodologies we use so that the results shown are reproducible and method replicable.

1.7.3 Stochastic simulations

The stochastic approach enabled the capture of variation in reservoir properties that is common across storage sites (Gibson-Poole et al., 2024). While this approach was taken for reasons of practicality and data availability, the two types of data set used have differing implications for the results from one another. For a dataset that contains more than one well, the results will be more representative of the target stratigraphy throughout the whole area. As the multi-variate distributions are derived from several wells within the same area, the variance in elastic properties of the target stratigraphy, and different logging tools are accounted for and incorporated within the model. For single-well datasets, while the results are not as applicable to a regional area, the stochastic approach taken does provide valuable insights into the uncertainty prediction for a highly localised area in and around the wellbore. Value is also gained when comparing the two datasets, using a wider range of data from which to generate distributions from allows for an indication of how reservoir heterogeneity may impact fluid substitution and hence seismic response.

1.7.4 Implications for hydrogen exploration and storage

While proposed native hydrogen source rock settings typically involve basement rocks and non-sedimentary basin-based processes, these generation pathways do not exclude the possibility of a sedimentary reservoir overlaying potential generation processes, and hence acting as a reservoir for the migration of native hydrogen into them (Jackson et al., 2024). Understanding the potential seismic response of hydrogen in porous materials can have applications in exploration in sedimentary sequences.

Our work shows that through forward modelling hydrogen, the elastic properties of a rock saturated with hydrogen are affected similarly to methane (natural gas) (Figure 3). Thus, geophysical exploration workflows used for predicting the likelihood of gas may be applicable to native hydrogen exploration.

Hydrogen in pore space gives a larger acoustic impedance change than carbon dioxide (Figure 5). This has implications for storage and management of hydrogen within the subsurface, as is proposed for areas of the UKCS or in salt caverns (Jahanbakhsh et al., 2024). Time-lapse (4D) seismic data can afford a valuable method for the monitoring of storage complexes (Morgan et al., 2020). Our work agrees with other more computationally intensive methods (e.g. Gao et al. (2024)) that ideally should be modelled and chosen, such that hydrogen within the pore space enables the 4% change in acoustic impedance required for 4D seismic detection. Hydrogen also shows greater change in AVO than carbon dioxide emphasising the need for careful survey design when consider time-lapse (4D) seismic for monitoring potential storage sites or detecting natural accumulations. We did not examine possible time shifts from hydrogen substituted into a sandstone reservoir. However, as hydrogen causes compressional velocity increases at relatively high water saturations (+80%) (Figure 3), we would expect a similar timeshift to that shown in Figure 12 and 13.

1.7.5 Future work and limitations

While the injection phase of carbon capture sites is typically expected to last decades, the migration and chemical reactions of carbon dioxide in the subsurface will continue for far longer (Metz et al., 2005). Most modelling scenarios consider carbon dioxide in the super critical phase just after injection, over longer time scale (>50 years) considerations need to be given to carbon dioxide dissolved within brine and any mineral precipitation. While these chemical reactions will take significant time, >10 years to dissolve into water, and >100 for the precipitation of carbonate minerals, an understanding of whether seismic methods could offer effective monitoring of these subsurface changes is essential. The modelling approach here could be extended to investigate different scenarios and the resulting elastic properties. Such models would investigate the elastic properties of brine with significant carbon dioxide dissolved within, and the host reservoir with carbonates precipitated within the pore space, both of which are likely to modify the elastic properties.

The most common seismic monitoring methods for oil and gas production (Djuraev et al., 2017) and for CCS projects (Ma et al., 2016) utilise active source reflection surveying, requiring baseline and monitor seismic surveys to map plume migration. Acquisition of monitor seismic surveys is a large expenditure for carbon capture sites, with typical individual survey costs being in the 10's of millions (Waal and Calvert, 2003). Other seismic monitoring methods that do not rely on follow up surveys may prove more cost-effective than these traditional techniques. Recent advances in both land and ocean bottom seismic receiver technology have allowed for the application of passive seismic techniques for monitoring purposes. Seismic arrays are typically deployed for an extended period of time, and as such the continuous records of ambient seismic noise can be used to develop subsurface imagery through interferometry (e.g. Cao and Askari (2019)), as well as for seismic event detection, location and characterisation (Verdon et al., 2010). Seismic event detection and characterisation is particularly important before, during and post-injection. It is possible to both distinguish whether detected seismic events are natural or induced and track the impact of injection on reservoir integrity (Payre et al., 2014). Passive seismic monitoring is regularly employed onshore, however applying these techniques offshore can be difficult due to the logistical challenges in dense instrument deployment and levels of ambient seismic noise offshore. To account for this, recent studies utilising passive seismic techniques for offshore monitoring have incorporated array processing techniques on a combination of both onshore broadband seismometers and offshore geophones, allowing for previously uncatalogued events to be detected (Zarifi et al., 2022; Jerkins et al., 2023). The modelled results here demonstrate changes in elastic properties that are equally as important when considering the application of passive seismic methods (Eisner et al., 2009). Further work could extend the modelling to consider whether the modelled changes in compressional velocity could be detected in different array configurations and noise environments (e.g, Stork et al. (2018)).

Our work on timeshifts does not account for the affects that heterogeneities such as thin beds may have. Thin beds and low frequencies can both cause tuning effects to occur within 4D seismic data sets (MacBeth et al., 2020), and if a thin bed is < tuning thickness can be assumed that the timeshift signal drops to 0 (MacBeth and Izadian, 2023). Characterisation of the heterogeneities within a storage complex and inclusion within the forward modelling workflow would allow for more accurate timeshift results.

The Q factor is the measure of attenuation observed within seismic waves (Jyothi et al., 2017). Changes in reservoir fluids have been shown to modify the value of Q (Joel et al., 2003). Measuring the Q factor within a 4D seismic dataset could provide viable ways to monitor change in carbon dioxide saturation within reservoirs.

1.7.6 Conclusions

We have used a stochastic Gassmann fluid substitution model to investigate the potential seismic response of potential storage reservoirs on the UKCS. We parametrise the models' using data from multiple wells to evaluate the implications of varying reservoir porosity of carbon dioxide and hydrogen on the elastic properties and hence geophysical responses.

Our results show that while seismic methods are valid for monitoring carbon dioxide plume migration, in key reservoir intervals on the UKCS likely changes in elastic properties, and acoustic impedance, may be lower than that reported and close to detection limits. Extra to relaying on 4D seismic and amplitude comparison, AVO and timeshift analysis may also be required to understand plume migration for geology where its acoustic impedance responses are calculated to be low (<4%).

We also calculate the results for hydrogen in the subsurface to understand responses of possible native hydrogen reservoirs or for hydrogen storage sites. Results for hydrogen show that it affects the elastic properties in a similar way to natural gas (from 100 to 0 % water saturation), and thus we can expect typical industry quantitative seismic techniques to be applicable for both the exploration of native hydrogen reserves and for the monitoring of hydrogen in storage.

We also discuss the difference in our results from published literature for the UKCS. While we cannot comment on the rightness of our results compared with those in published reports for target CCS sites, we can be open and transparent with our scientific practices, making all our code and input data available at the time of publication. We suggest that this should be the case for subsurface infrastructure of national importance, especially when CCS sites are government-funded and not-for-profit activities, as it allows for proper scrutiny and scientific process to be undertaken.

1.8 Tables

Reservoir	Assumed depth (m)	Pressure (MPa)	Temperature (c)	Density (Kg/m^3)	Bulk modulus (Gpa)
Leman	2447	30.4	72.5	173.6 (Methane) 18.3 (Hydrogen) 781 (Carbon dioxide)	0.068 (Methane) 0.050 (Hydrogen) 0.199 (Carbon dioxide)
Bunter	1406	15.2	57	100 (Methane) 10.3 (Hydrogen) 641 (Carbon dioxide)	.024 (Methane) .023 (Hydrogen) .068 (Carbon dioxide)
Helsby	792	9.68	30	71.2 (Methane) 7.3 (Hydrogen) 763 (Carbon dioxide)	.014 (Methane) .014 (Hydrogen) .105 (Carbon dioxide)

TABLE 1 – FLUID ELASTIC PROPERTIES AT RESERVOIR CONDITIONS FOR LEMAN, BUNTER AND HELSBY FORMATIONS

Cut off parameter	Minimum Value	Maximum Value
Volume Shale (Vshale)	0%	30%
Porosity (Φ)	5%	NaN
Bulk density (ρ_{bulk})	2.00 g/cm^3	2.67 g/cm^3

TABLE 2 – RESERVOIR CUTOFF VALUES FROM DIFFERENT ROCK PROPERTIES

Formation	Stochastic Porosity Groups (Φ%)
Leman	7, 9, 11, 13, 15, 17, 19
Helsby	14, 16, 18, 20, 22, 24, 26
Bunter	19, 21, 23, 25, 27

TABLE 3 – POROSITY GROUPS OF CHOSEN STRATIGRAPHY FOR STOCHASTIC ANALYSIS

Stratigraphy	Calculated AI Change p50 (Water saturation 20 %)	Literature Ai change	Calculated AVO (Rc) % Change Difference between Near stack – Far stack offsets	Timeshift	Notes
Leman (Φ 15)	-8 (Figure 5)	Not quantified but 'Very poor' (James et al., 2016b)	Res – Res: 38.2 Seal – Res: 22.2	Nan	Seal (Zechstein) may cause an issue
Bunter (Φ 23)	-6 (Figure 6)	12 – 20% (BEIS, 2021)	Res – Res: 25.4 Seal – Res (Claystone): 4.48 Seal – Res (Evaporite):-23.5	0.877ms (Figure 12)	No data given by (BEIS, 2021) on how value calculated,
Helsby (Φ 16)	-2 (Figure 7)	Not quantified, but 'Maybe detectable' at 60% carbon dioxide saturation (Green and Grammer, 2016)	Res – Res: -3.32 Seal – Res:0.91	Nan	

TABLE 4 INVESTIGATED STRATIGRAPHY WITH RESULTS FOR SELECT POROSITY. RESULTS FROM THE LITERATURE ARE ALSO PRESENT

1.9 Appendix

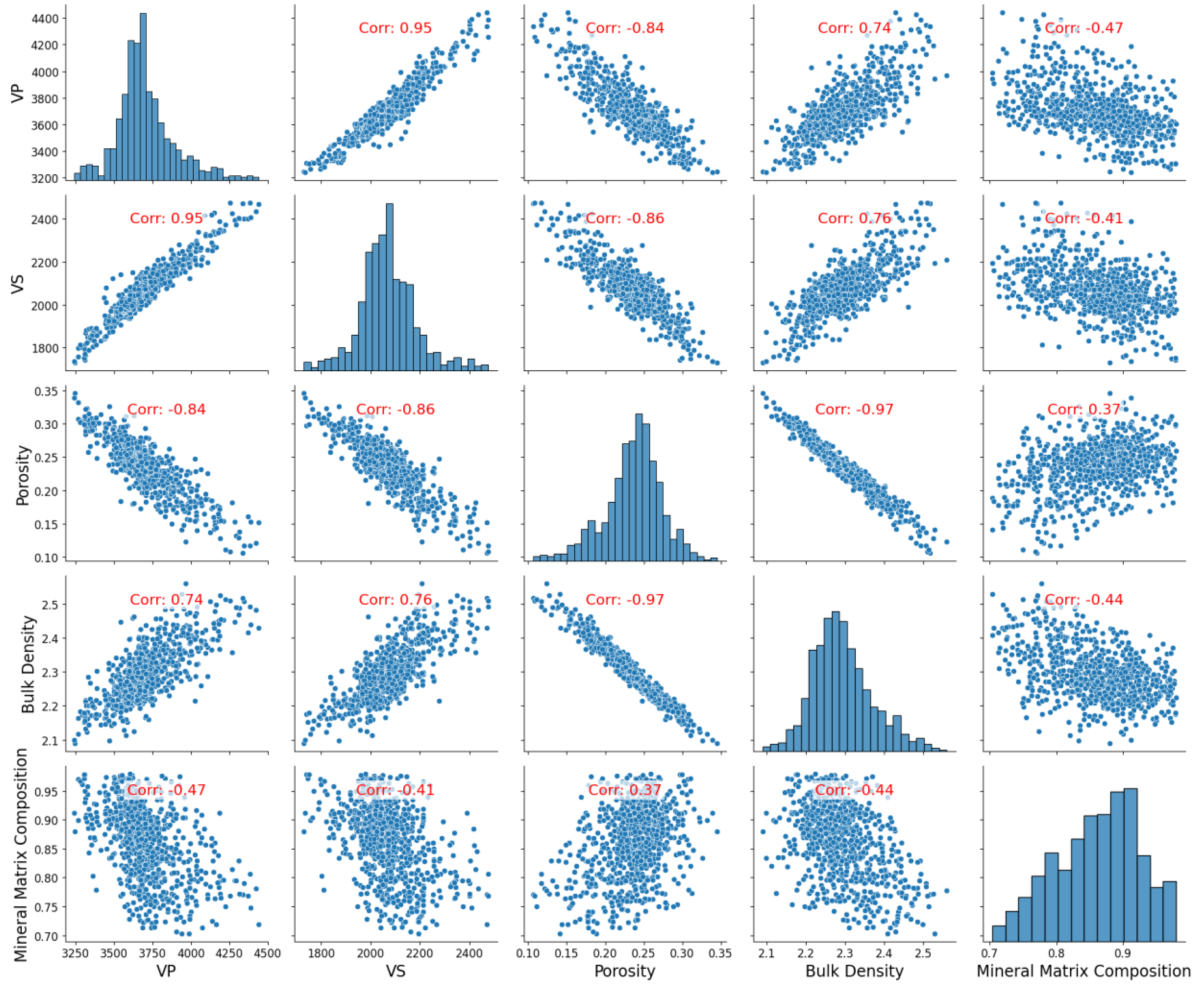

Appendix 1 Cross plot of well elastic and mineralogical properties of the Bunter sandstone reservoir section from well 42/25-D3

Well	Formation	Depth
42/25d-3	Bunter SST	1406 - 1538 m
110/13b-21	Helsby SST	2600 - 2680 m
43/28a-3	Leman SST	
44/23b-11	Leman SST	
44/27-1	Leman SST	
47/10-8	Leman SST	
48/12a-7Z	Leman SST	
48/2b-3	Leman SST	
49/20a-7	Leman SST	
49/28-18	Leman SST	

Appendix 2 Well data utilised within study

1.10 Acknowledgements

1.10.1 Author contributions

Barnett (conceptualization, data curation, formal analysis, investigation methodology, project administration, visualisation, writing – original draft, writing – review and editing), Ireland (conceptualization, funding acquisition, supervision, writing – review and editing), Van der Land (supervision, writing – review and editing), Dunham (writing – review and editing)

1.10.2 Funding information

Hector Barnett's PhD is funded through the Centre for Doctoral Training (CDT) in Geoscience and the Low Carbon Energy Transition.

1.10.3 Data availability

All data generated and code used within this manuscript is available at https://figshare.com/s/01c10efe1839c03c28ff

Well data were provided by the North Sea Transition Authority under an Open Government Licence. Data were interpreted using SLB's Petrel and Techlog software which was provided under an academic licence.

1.11 Bibliography

Agile-Scientific. (2022). *bruges 0.5.4*. In https://pypi.org/project/bruges/

Ahmed, N., Khalid, P., Ghazi, S., & Anwar, A. W. (2015). AVO forward modeling and attributes analysis for fluid's identification: a case study. *Acta Geodaetica et Geophysica*, *50*(4), 377-390. https://doi.org/10.1007/s40328-014-0097-x

Anston-Race, S. E., & Ganesh, D. (2020). The Viking Fields, Blocks 49/11d, 49/12a, 49/16a, 49/16c, 49/17a, UK North Sea. *Geological Society, London, Memoirs*, *52*(1), 273-287. https://doi.org/10.1144/M52-2018-55

Avseth, P., Mukerji, T., & Mavko, G. (2005). *Quantitative Seismic Interpretation: Applying Rock Physics Tools to Reduce Interpretation Risk*. Cambridge University Press. https://doi.org/https://doi.org/10.1017/CBO9780511600074

Bachmann, Geluk, M., Warrington, Becker-Roman, Beutler, Hagdorn, Hounslow, Nitsch, Rohling, Simon, & Szulc. (2010). Chapter 9: Triassic. In H. Doornenbal & A. Stevenson (Eds.), *Petroleum Geological Atlas of the Southern Permian Basin Area*.

Bacon, M., Simm, R., & Redshaw, T. (2003). 3-D Seismic Interpretation. In. Cambridge University Press. https://doi.org/doi.org/10.1017/CBO9780511802416

Bahmaei, Z., & Hosseini, E. (2020). Pore pressure prediction using seismic velocity modeling: case study, Sefid-Zakhor gas field in Southern Iran. *Exploration Geophysics*. https://doi.org/https://doi.org/10.1007/s13202-019-00818-y

Batzle, M., & Wang, Z. (1992). Seismic properties of pore fluids. *Geophysics*, *57*(11), 1396-1408. https://doi.org/10.1190/1.1443207

BEIS, D. o. B. E. a. I. S. (2021). *Measurement Monitoring and Verification (MMV) Plan for Endurance*

Bentham, M. S., Green, A., & Gammer, D. (2013). The Occurrence of Faults in the Bunter Sandstone Formation of the UK Sector of the Southern North Sea and the Potential Impact on Storage Capacity. *Energy Procedia*, *37*, 5101-5109. https://doi.org/10.1016/j.egypro.2013.06.423

Blow, R. A., & Hardman, M. (2022). Calder Field appraisal well 110/7a-8, East Irish Sea Basin. *Geological Society, London, Special Publications*, *124*(1), 387-397. https://doi.org/10.1144/gsl.Sp.1997.124.01.23

British Geological Survey. (2020). *The BGS Lexicon of Named Rock Units [online]*. https://www.bgs.ac.uk/technologies/the-bgs-lexicon-of-named-rock-units/.

Brook, M., Shaw, K., Vincent, C., & Holloway, S. (2003). *Gestco case study 2a-1: Storage Potential of the Bunter Sandstone in the UK sector of the southern North Sea and the adjacent onshore area of Eastern England*.

Cao, H., & Askari, R. (2019). Comparison of seismic interferometry techniques for the retrieval of seismic body waves in CO2 sequestration monitoring. *Journal of Geophysics and Engineering*, *16*(6), 1094-1115. https://doi.org/10.1093/jge/gxz079

Carpentier, S., Boullenger, B., & Barros, E. (2021). CCS Monitoring by Inversion of Reservoir Pressure and Saturation Changes from Timelapse AVO Differences and Time-Shifts. *82nd EAGE Annual Conference & Exhibition*. https://doi.org/https://doi.org/10.3997/2214-4609.202011837

Castagna, J., Batzle, M., Kan, T., & Backus, M. (1993). Rock physics—The link between rock properties and AVO response. *Offset-dependent reflectivity—Theory and practice of AVO analysis: SEG*, *8*, 135-171.

Chadwick, R. A., Arts, R., & Eiken, O. (2005). 4D seismic quantification of a growing CO2 plume at Sleipner, North Sea. *Geological Society, London, Petroleum Geology Conference series*, *6*(1), 1385-1399. https://doi.org/10.1144/0061385

Chopra, S., & Castagna, J. (2014). Chapter 4: Zoeppritz Equations and their Approximations. In *AVO*. Tulsa, Oklahoma : Society of Exploration Geophysicists.

Clery, D., & Gough, C. (2022). Cluster Mapping Report: Hynet Northwest (NW industrial cluster).

Danesh, A. (1998). PVT and Phase Behaviour Of Petroleum Reservoir Fluids. In: Elsevier.

Darling, T. (2005). *Well Logging and Formation Evaluation*. Gulf Professional Publishing. https://doi.org/https://doi.org/10.1016/B978-0-7506-7883-4.X5000-1

de Jonge-Anderson, I., & Underhill, J. R. (2022). Use of Subsurface Geology in Assessing the Optimal Co-Location of CO2 Storage and Wind Energy Sites. *Earth Science, Systems and Society*, *2*. https://doi.org/10.3389/esss.2022.10055

Djuraev, U., Jufar, S. R., & Vasant, P. (2017). A review on conceptual and practical oil and gas reservoir monitoring methods. *Journal of Petroleum Science and Engineering*, *152*, 586-601. https://doi.org/10.1016/j.petrol.2017.01.038

Dowdell, B. L. (2020). *PySeisTuned2.0*. In https://www.pyseistuned.com/

Dupuy, B., C, V. A. T., Ghaderi, A., Querendez, E., & Mezyk, M. (2017). Constrained AVO for CO2 Storage Monitoring at Sleipner. *Energy Procedia*, *114*, 3927-3936. https://doi.org/10.1016/j.egypro.2017.03.1524

Dvorkin, J., Gutierrez, M., & Grana, D. (2014). *Seismic Reflections of Rock Properties*. Cambridge University Press. https://doi.org/https://doi.org/10.1017/CBO9780511843655

Dvorkin, J., Mavko, G., & Gurevich, B. (2007). Fluid substitution in shaley sediment using effective porosity. *Geophysics*, *72*(3), O1-O8. https://doi.org/10.1190/1.2565256

Eisner, L., Duncan, P. M., Heigl, W. M., & Keller, W. R. (2009). Uncertainties in passive seismic monitoring. *The Leading Edge*, *28*(6), 648-655. https://doi.org/10.1190/1.3148403

Gao, K., Creasy, N. M., Huang, L., & Gross, M. R. (2024). Underground hydrogen storage leakage detection and characterization based on machine learning of sparse seismic data. *International Journal of Hydrogen Energy*, *61*, 137-161. https://doi.org/10.1016/j.ijhydene.2024.02.296

Gassmann, F. (1951). Uber die Elastizitat Poroser Medien. In *Veirteljahrsschrift der Naturforschenden Gesellschaft in Zzirich* (Vol. 96, pp. 1 - 23).

Gast, R., Dusar, M., Breitkreuz, C., Gaupp, R., Schneider, J. W., Stemmerik, L., Geluk, M., Geißler, M., Glennie, K., Kabel, S., & Jones, N. (2010). Chapter 7 Rotliegend. In H. Doornenbal & A. Stevenson (Eds.), *Petroleum Geological Atlas of the South Permian Basin Area*.

Gibson-Poole, C. M., Taplin, M., Bouffin, N., Duffy, L., Sutherland, F., Cabral, A., & Ashby, D. (2024). Site Characterization of the Endurance CO2 Store, Southern North Sea, UK. *Geoenergy*, *0*(ja), geoenergy2024-2012. https://doi.org/10.1144/geoenergy2024-012

Glennie, K. W. (1998). *Petroleum Geology of the North Sea: Basic Concepts and Recent Advances* (4 ed.). Blackwell Scoence. https://doi.org/10.1002/9781444313413

Glennie, K. W., & Underhill, J. R. (1998). Origin, Development and Evolution of Structural Styles. In *Petroleum Geology of the North Sea* (pp. 42-84). https://doi.org/https://doi.org/10.1002/9781444313413.ch2

Gluyas, J. G., & Bagudu, U. (2020). The Endurance CO2 storage site, Blocks 42/25 and 43/21, UK North Sea. *Geological Society, London, Memoirs*, *52*(1), 163-171. https://doi.org/10.1144/M52-2019-47

Green, A., & Grammer, D. (2016). *Strategic UK CCS Storage Appraisal - WP5C - Hamilton Storage Development Plan* (Strategic UK CCS Storage Appraisal, Issue.

Harvey, S., Hopkins, J., Kuehl, H., O'Brien, S., & Mateeva, A. (2022a). Quest CCS facility: Time-lapse seismic campaigns. *International Journal of Greenhouse Gas Control*, *117*, 103665. https://doi.org/https://doi.org/10.1016/j.ijggc.2022.103665

Harvey, S., Hopkins, J., Kuehl, H., O'Brien, S., & Mateeva, A. (2022b). Quest CCS facility: Time-lapse seismic campaigns. *International Journal of Greenhouse Gas Control*, *117*. https://doi.org/10.1016/j.ijggc.2022.103665

Howard, A. S., Warrington, G., Ambrose, K., & Rees, J. G. (2008). *A formational framework for the Mercia Mudstone Group (Triassic) of England and Wales*.

Jack, D. I., Jackson, A. A., Evans, D., Wingfield, R. T. R., Barnes, R. P., & Arthuer, M. J. (1995). *The geology of the Irish Sea*.

Jackson, O., Lawrence, S. R., Hutchinson, I. P., Stocks, A. E., Barnicoat, A. C., & Powney, M. (2024). Natural hydrogen: sources, systems and exploration plays. *Geoenergy*, *2*(1). https://doi.org/10.1144/geoenergy2024-002

Jahanbakhsh, A., Louis Potapov-Crighton, A., Mosallanezhad, A., Tohidi Kaloorazi, N., & Maroto-Valer, M. M. (2024). Underground hydrogen storage: A UK perspective. *Renewable and Sustainable Energy Reviews*, *189*. https://doi.org/10.1016/j.rser.2023.114001

James, A., Baines, S., & McCollough, S. (2016a). *Strategic UK CCS Storage Appraisal - WP5A - Bunter Storage Development Plan*.

James, A., Baines, S., & McCollough, S. (2016b). *Strategic UK CCS Storage Appraisal - WP5E - Viking A Storage Development Plan*.

Jerkins, A. E., Köhler, A., & Oye, V. (2023). On the potential of offshore sensors and array processing for improving seismic event detection and locations in the North Sea. *Geophysical Journal International*, *233*(2), 1191-1212. https://doi.org/10.1093/gji/ggac513

Joel, W., Taner, M. T., Naum, D., Gary, M., & Jack, D. (2003). *SEISMIC ATTENUATION FOR RESERVOIR CHARACTERIZATION*. https://www.osti.gov/biblio/834365

Jyothi, V., Sain, K., Pandey, V., & Bhaumik, A. (2017). Seismic Attenuation for Characterization of Gas Hydrate Reservoir in Krishna-Godavari Basin, Eastern Indian Margin. *JOURNAL GEOLOGICAL SOCIETY OF INDIA*, *90*, 261-266.

Kennedy, M. (2015). *Practical petrophysics*. Amsterdam : Elsevier.

Kirk, K. L. (2005). *Potential for storage of carbon dioxide in the rocks beneath the East Irish Sea* (CR/05/127N).

Leachman, J. W., Jacobsen, R. T., Penoncello, S. G., & Lemmon, E. W. (2009). Fundamental Equations of State for Parahydrogen, Normal Hydrogen, and Orthohydrogen. *Journal of Physical and Chemical Reference Data*, *38*(3), 721-748. https://doi.org/10.1063/1.3160306

Lumley, D. E., & Behrens, R. A. (1998). Practical Issues of 4D Seismic Reservoir Monitoring: What an Engineer Needs to Know. *SPE Reservoir Evaluation & Engineering*, *1*(06), 528-538. https://doi.org/10.2118/53004-pa

Ma, J.-F., Li, L., Wang, H.-F., Tan, M.-Y., Cui, S.-L., Zhang, Y.-Y., Qu, Z.-P., Jia, L.-Y., & Zhang, S.-H. (2016). Geophysical monitoring technology for CO2 sequestration. *Applied Geophysics*, *13*(2), 288-306. https://doi.org/10.1007/s11770-016-0553-1

MacBeth, C., Amini, H., & Izadian, S. (2020). Review Paper: Methods of measurement for 4D seismic post-stack time shifts. *Geophysical Prospecting*, *68*(9), 2637-2664. https://doi.org/10.1111/1365-2478.13022

MacBeth, C., & Izadian, S. (2023). A review and analysis of errors in post-stack time-shift interpretation. *Geophysical Prospecting*, *71*(8), 1497-1522. https://doi.org/https://doi.org/10.1111/1365-2478.13391

MacBeth, C., Mangriotis, M. D., & Amini, H. (2018). Review Paper: Post-stack 4D seismic time-shifts: Interpretation and evaluation. *Geophysical Prospecting*, *67*(1), 3-31. https://doi.org/10.1111/1365-2478.12688

Marelli, S., & Sudret, B. (2014). UQLab: A Framework for Uncertainty Quantification in Matlab. In *Vulnerability, Uncertainty, and Risk* (pp. 2554-2563). https://doi.org/doi:10.1061/9780784413609.257

Mavko, G., Mukerji, T., & Dvorkin, J. (2009). *The Rock Physics Handbook: Tools for Seismic Analysis of Porous Media*. Cambridge University Press. https://doi.org/https://doi.org/10.1017/CBO9780511626753

Metz, B., Davidson, O., Coninck, H. d., Loos, M., & Meyer, L. (2005). *Carbon Dioxide Capture and Storage*.

Morgan, E., Garden, M., Egreteau A, Boubaker, Y., Gestin, K., & Mari, J. L. (2020). Focused and Continuous Ultra-Light Seismic Monitoring: A Gas Storage Example. *EAGE 2020 Annual Conference & Exhibition Online* https://doi.org/https://doi.org/10.3997/2214-4609.202010495

Mosegaard, K. (2023). Monte Carlo method. In *Encyclopedia of Mathematical Geosciences* (pp. 890-896). Springer.

NIST Chemistry WebBook. (1997). *NIST Chemistry WebBook*.

Nolen-Hoeksema, R. C. (2000). Modulus—porosity relations, Gassmann's equations, and the low-frequency elastic-wave response to fluids. *Geophysics*, *65*(5), 1355-1363. https://doi.org/10.1190/1.1444826

Okere, C. J., Sheng, J. J., & Ejike, C. (2024). Evaluating reservoir suitability for large-scale hydrogen storage: A preliminary assessment considering reservoir properties. *Energy Geoscience*, *5*(4), 100318. https://doi.org/https://doi.org/10.1016/j.engeos.2024.100318

Peryt, T., Geluk, M., Mathiesen, M., Paul, J., & Smith, K. (2010). Chapter 8 Zechstein. In H. Doornenbal & A. Stevenson (Eds.), *Petroleum Geological Atlas of the South Permian Basin Area*.

Pradhan, A., Dutta, N. C., Le, H. Q., Biondi, B., & Mukerji, T. (2020). Approximate Bayesian inference of seismic velocity and pore-pressure uncertainty with basin modeling, rock physics, and imaging constraints. *Geophysics*, *85*(5), ID19-ID34. https://doi.org/10.1190/geo2019-0767.1

Qin, X., Han, D. H., & Zhao, L. (2022). Measurement of Grain Bulk Modulus on Sandstone Samples From the Norwegian Continental Shelf. *Journal of Geophysical Research: Solid Earth*, *127*(9). https://doi.org/10.1029/2022jb024550

Ringrose, P. S., & Bentley, M. (2021). *Reservoir Model Design; A Practitioner's Guide*. Springer Nature Link.

Rouillard, P., Bagley, G., Moseley, D., Myers, K., & Harding, A. (2020). UKCS exploration: 50 years and counting. *Geological Society, London, Memoirs*, *52*(1), 32-42. https://doi.org/10.1144/m52-2018-66

Salemi, H., Iglauer, S., Rezagholilou, A., & Sarmadivaleh, M. (2018). Laboratory measurement of Biot's coefficient and pore pressure influence on poroelastic rock behaviour. *The APPEA Journal*, *58*(1), 182-189. https://doi.org/10.1071/AJ17069

Scorgie, J. C., Worden, R. H., Utley, J. E. P., & Roche, I. P. (2021). Reservoir quality and diagenesis of Triassic sandstones and siltstones from arid fluvial and playa margin environments: A study of one of the UK's earliest producing oilfields. *Marine and Petroleum Geology*, *131*. https://doi.org/10.1016/j.marpetgeo.2021.105154

Setzmann, U., & Wagner, W. (1991). A New Equation of State and Tables of Thermodynamic Properties for Methane Covering the Range from the Melting Line to 625 K at Pressures up to 1000 MPa. *Journal of Physical and Chemical Reference Data*, *20*(6), 1061-1155. https://doi.org/10.1063/1.555898

Singer, L., Byerley, G., & Rose, P. (2018). Re-saturation targets identified from 4D seismic softening responses in the Forties Field. *Geological Society, London, Petroleum Geology Conference series*, *8*(1), 473-483. https://doi.org/10.1144/PGC8.25

Smith, T. M., Sondergeld, C. H., & Rai, C. S. (2003). Gassmann fluid substitutions: A tutorial. *Geophysics*, *68*(2), 430-440. https://doi.org/10.1190/1.1567211

Soboĺ, I. (1993). Sensitivity estimates for nonlinear mathematical models. *Math. Model. Comput. Exp.*, *1*, 407.

Span, R., & Wagner, W. (1996). A New Equation of State for Carbon Dioxide Covering the Fluid Region from the Triple-Point Temperature to 1100 K at Pressures up to 800 MPa. *Journal of Physical and Chemical Reference Data*, *25*(6), 1509-1596. https://doi.org/10.1063/1.555991

Steventon, M. J., Jackson, C. A. L., Hall, M., Ireland, M. T., Munafo, M., & Roberts, K. J. (2022). Reproducibility in Subsurface Geoscience. *Earth Science, Systems and Society*, *2*. https://doi.org/10.3389/esss.2022.10051

Stork, A. L., Allmark, C., Curtis, A., Kendall, J. M., & White, D. J. (2018). Assessing the potential to use repeated ambient noise seismic tomography to detect CO2 leaks: Application to the Aquistore storage site. *International Journal of Greenhouse Gas Control*, *71*, 20-35. https://doi.org/10.1016/j.ijggc.2018.02.007

Stuart, I. A. (1991). The Rough Gas Storage Field, Blocks 47/3d, 47/8b, UK North Sea. *Geological Society, London, Memoirs*, *14*(1), 477-484. https://doi.org/10.1144/gsl.Mem.1991.014.01.59

UK Government. (2024). *NSTA awards Endurance first ever UK carbon storage permit*. https://www.nstauthority.co.uk/news-publications/nsta-awards-endurance-first-ever-uk-carbon-storage-permit/

Verdon, J. P., Kendall, J. M., White, D. J., Angus, D. A., Fisher, Q. J., & Urbancic, T. (2010). Passive seismic monitoring of carbon dioxide storage at Weyburn. *The Leading Edge*, *29*(2), 200-206. https://doi.org/10.1190/1.3304825

Waal, H. d., & Calvert, R. (2003). Overview of global 4D seismic implementation strategy. *Petroleum Geoscience*, *9*(1), 1-6. https://doi.org/doi:10.1144/1354-079302-531

Wandler, A., Evans, B., & Link, C. (2007). AVO as a fluid indicator: A physical modeling study. *Geophysics*, *72*(1), C9-C17. https://doi.org/10.1190/1.2392817

Yaliz, A., & Taylor, P. (2003). The Hamilton and Hamilton North Gas Fields, Block 110/13a, East Irish Sea. *Geological Society, London, Memoirs*, *20*. https://doi.org/https://doi.org/10.1144/GSL.MEM.2003.020.01.0

Yan, H., Dupuy, B., Romdhane, A., & Arntsen, B. (2018). CO2 saturation estimates at Sleipner (North Sea) from seismic tomography and rock physics inversion. *Geophysical Prospecting*, *67*(4), 1055-1071. https://doi.org/10.1111/1365-2478.12693

Zarifi, Z., Köhler, A., Ringrose, P., Ottemöller, L., Furre, A.-K., Hansteen, F., Jerkins, A., Oye, V., Dehghan Niri, R., & Bakke, R. (2022). Background Seismicity Monitoring to Prepare for Large-Scale CO2 Storage Offshore Norway. *Seismological Research Letters*, *94*(2A), 775-791. https://doi.org/10.1785/0220220178

Zhang, J. (2020). Modern Monte Carlo methods for efficient uncertainty quantification and propagation: A survey. *WIREs Computational Statistics*, *13*(5). https://doi.org/10.1002/wics.1539

Ziegler, P. A. (1990). *Geological Atlas of Central and Western Europe* (2nd ed.). The Hague : Shell International Petroleum Maatschappij B.V.

Ziegler, P. A. (1992). North Sea rift system. *Tectonophysics*, *208*(1), 55-75. https://doi.org/https://doi.org/10.1016/0040-1951(92)90336-5

Zoeppritz, K. (1919). VIIb. Über Reflexion und Durchgang seismischer Wellen durch Unstetigkeitsflächen. *Nachrichten von der Königlichen Gesellschaft der Wissenschaften zu Göttingen*, 66-84.